Carbon emissions and radiative forcings from tundra wildfires in the Yukon-Kuskokwim River Delta, Alaska

Michael Moubarak[1], Seeta Sistla[2], Stefano Potter[3], Susan M. Natali[3,*], Brendan M. Rogers[3,*]

[1]Department of Biology, Hamilton College, Clinton, NY 13323, United States
[2]Department of Natural Resources and Environmental Sciences, California Polytechnic State University, San Luis Obispo, CA 93407, United States
[3]Woodwell Climate Research Center, Falmouth, MA 02540, United States

Correspondence to: Michael Moubarak (moubarak.michael@gmail.com)
*Equal last authorship

Abstract

Tundra environments are experiencing elevated levels of wildfire, and the frequency is expected to keep increasing due to rapid climate change in the Arctic. Tundra wildfires can release globally significant amounts of greenhouse gasses that influence the Earth's radiative balance. Here we develop a novel method for estimating carbon loss and the resulting radiative forcings of gaseous and aerosol emissions from 2015 tundra wildfires in the Yukon-Kuskokwim Delta (YKD), Alaska. We paired burn depth measurements using two vegetative reference points that survived the fire event —*Sphagnum fuscum* and *Dicranum spp.*— with measurements of local organic matter and soil carbon properties to estimate total ecosystem organic matter and carbon loss. We used remotely-sensed data on fire severity from Landsat 8 to scale our measured losses to the entire fire-affected area, with an estimated total loss of 2.04 Tg of organic matter and 0.91 Tg of carbon, and an average loss of 3.76 kg m^{-2} of organic matter and 1.68 kg m^{-2} of carbon in the 2015 YKD wildfires. To demonstrate the impact of these fires on Earth's radiation budget, we developed a simple but comprehensive framework to estimate the radiative forcing from Arctic wildfires. We synthesized existing research on the lifetime and radiative forcings of gaseous and aerosol emissions of CO_2, N_2O, CH_4, O_3 and its precursors, and fire aerosols. The model shows a net positive cumulative mean radiative forcing of 3.67 W m^{-2} using RCP 4.5 and 3.37 W m^{-2} using RCP 8.5 at 80 years post-fire, which was dominated by CO_2 emissions. Our results highlight the climate impact of tundra wildfires, which positively reinforce climate warming and increased fire frequency through the radiative forcings of their gaseous emissions.

1 Introduction

The Arctic region is characterized by permafrost soils with low rates of decomposition and high carbon content from millennia of positive net ecosystem production (NEP; Lindgren et al., 2018). As a result, there is more than twice as much carbon stored in permafrost soils as there is in the atmosphere, including roughly 1,035 ± 150 Pg of carbon in the top three meters of soil (Schuur et al., 2015). Surface air temperatures in the Arctic have been increasing more than twice as fast as the global average since the mid-20th century (Cohen et al., 2018) and are expected to continue increasing with more variable precipitation, hence more frequently pairing hot and dry conditions (IPCC, 2021; Hu et al., 2015). Changing environmental conditions will place some of this large carbon stock at risk for release into the atmosphere through increased biological activity and wildfire (Natali et al., 2019, Natali et al., 2015, Rocha et al., 2011a, Hu et al., 2010).

62   Fires are an increasingly important component of tundra carbon cycling. Fires are becoming more frequent

63   in Arctic systems due to increasing occurrences of hot and dry conditions coupled with more lightning ignitions

64   (Chen et al., 2021, Bieniek et al., 2020, Veraverbeke et al., 2017b). For example, the 2007 Anaktuvuk River

65   megafire on the North Slope of Alaska occurred during an especially hot and dry period and released an amount of

66   carbon similar in magnitude to annual sequestration across the entire tundra biome (Mack et al., 2011). Continued

67   and potentially accelerated rates of warming are expected to further increase the frequency of tundra wildfires,

68   thereby releasing significant amounts of carbon and altering the net carbon balance of the tundra biome (Hu et al.,

69   2015).

70   A recent body of literature indicates the potential to estimate wildfire carbon emissions in boreal forests by

71   linking geospatial predictors, most prominently satellite-derived estimates of fire severity and extent, with *in situ*

72   measurements of carbon loss (e.g. Dieleman et al., 2020, Walker et al., 2018b, Veraverbeke et al., 2015b, and

73   Rogers et al., 2014). Despite increasing incidence of tundra wildfires, these studies have primarily focused on boreal

74   forests, and few estimates are available for tundra (Mack et al., 2011). Whereas satellite-derived fire extent and

75   severity is widely available, representative *in situ* measurements of tundra wildfires are not. *In situ* measurements of

76   fire effects on tundra organic soils are challenging due to a lack of reference points (e.g., adventitious roots) that

77   survive the fire, which are used to estimate pre-fire organic matter depth and content (Walker et al., 2018a, Rogers et

78   al., 2014, Boby et al., 2010). Measurements of organic matter loss must also be region-specific because of

79   differences in vegetation and soil properties (Walker et al., 2020c, Mack et al., 2011).

80   Although carbon loss estimates from Arctic wildfires are important for understanding the impacts of

81   climate change on carbon budgets, radiative forcings from wildfire gaseous and aerosol emissions are needed to

82   properly gauge the impact on the Earth's atmosphere and climate (Huang et al., 2016, Ward et al., 2012, Randerson

83   et al., 2006). Radiative forcings from wildfires depend spatially on fire severity and atmospheric conditions and

84   temporally on changing atmospheric background concentrations in the months, years, and decades following the fire

85   (Huang et al., 2016, Joos et al., 2013). To date, radiative forcings from high-latitude wildfires have been estimated

86   for particular boreal forests (Huang et al., 2016, O'Halloran et al., 2012, Randerson et al., 2006) and within global

87   models (Ward et al., 2012), but not for tundra ecosystems.

88   Here we take a two-step approach to assess the impact of tundra wildfires on carbon budgets and climate.

89   We first developed a method for measuring carbon loss *in situ* in tundra ecosystems, particularly for the 2015 fire

90   season in the Yukon-Kuskokwim Delta, AK. We tested the agreement of multiple pre-fire reference points for

91   estimating burn depth in the field and combined these estimates with laboratory-measured organic matter and carbon

92   fractions to estimate emissions. We then used 30m remotely-sensed fire severity data (differenced Normalized Burn

93   Ratio, or dNBR; Key and Benson, 2006) from Landsat 8 to scale our measurements to the entire fire area. Finally,

94   we estimated the long-term radiative forcings of the fire season's gaseous and particulate emissions, including long-

95   lived greenhouse gasses (GHGs), ozone, ozone precursors, and aerosols, using a variety of published algorithms and

96   arctic-specific parameters when available.

97   **2 Materials and Methods**

98   **2.1 Study Area**

99   Field measurements were collected in the summer of 2019 in a burn scar from the 2015 fire season in the

100   Yukon-Kuskokwim Delta, AK (YKD; Fig. 1). The burn scar we sampled was adjacent to an uninhabited but

101   regularly accessed Arctic field research outpost in the YKD established in 2016. Base camp was situated at 61.2632

102   °N, 163.2458 °W, approximately 95 kilometers northwest of Bethel, AK, accessible by float plane and helicopter.

103   Sampling was done within about an 11-kilometer radius of the base camp (Fig. 1c). Measurements from the field

104   were scaled to all fire scars in the YKD that burned in 2015 (Fig. 1b). We used fire perimeters from the Alaska

105   Large Fire Database (ALFD; Kasischke et al., 2002).

106

107
108 **Figure 1.** (a) The location of the YKD within Alaska, (b) the areas of fires in 2015 within the YKD, and (c) the
109 locations of our vegetative reference point height transects in burned and unburned areas within about an 11 km
110 radius from base camp. Fire perimeters were derived from the Alaska Large Fire Database (Kasischke et al., 2002).
111 Sources: Esri, DigitalGlobe, GeoEye, i-cubed, USDA FSA, USGS, AEX, Getmapping, Aerogrid, IGN, IGP,
112 swisstopo, and the GIS User Community.
113
114   The YKD contains tussock-sedge, dwarf-shrub, and lichen and moss tundra communities over ice-rich

115 permafrost peat plateaus (Raynolds et al., 2005). These peat plateaus were the primary land component burned in

116 the wildfires and were separated by fens, bogs, and open water. Within our sample area, lichen was the dominant

117 vegetation type (Frost et al., 2020), shrubs were interspersed across the landscape, and tussocks were rare. Soil is

118 predominantly organic (Jorgenson et al., 2000), which has accumulated over sand deposits from the Pleistocene

119 period (Shaw, 1998).

120 **2.2 Fire severity**

121   Fire perimeters in the YKD in 2015 were extracted from the ALFD. We used a remotely sensed metric of

122 fire severity from Landsat 8 Tier 1 surface reflectance imagery: dNBR (Eq. 1), which is based on the Normalized

123 Burn Ratio (NBR; Eq. 2; Key and Benson, 2006). Clouds, cloud shadows, and snow were masked from all images

124 using the provided pixel quality attributes generated from the CFMASK algorithm (Foga et al., 2017). Imagery for

125 this index was acquired as the mean Landsat 8 composite between June 1st and August 31st for one year pre- and one

126 year post-fire, and for all fire scars. All remotely sensed variables were extracted in Google Earth Engine (Gorelick

127 et al., 2017). Where in Eq. (2) NIR is near-infrared (Band 5) and SWIR is shortwave infrared (Band 7).

128 $dNBR = (NBR_{prefire} - NBR_{postfire}) \times 1000,$ (1)

129 $NBR = \frac{(NIR-SWIR)}{(SWIR+NIR)},$ (2)

130 We compared dNBR from the YKD 2015 fire season to all fires in boreal and tundra Alaska to place the

131 measured dNBR in context. Using fire records from the ALFD, dNBR was acquired for all available fire perimeters

132 in Alaska. Differenced NBR was calculated in the same way as described before, but with the exception that

133 Landsat 4, 5, 7, and 8 were used in the pre and post-fire composites. Due to differences in spectral bands, Landsat 8

134 was corrected to match Landsat 7 using a regression technique (Roy et al., 2016). The first fire year we detected

135 dNBR was in 1989 and the most recent was in 2019. Boreal and tundra extents were defined using the United States

136 Environmental Protection Agency ecoregions, with tundra as level one class 2.0 and boreal as level one classes 3.0

137 and 6.0 (U.S. Environmental Protection Agency, 2010).

138 **2.3 Vegetative marker height measurements**

139 We measured the height of vegetative reference points above the surface in both unburned and burned

140 areas. Three main dominant surface vegetative reference points were available: *Sphagnum fuscum, Dicranum spp.,*

141 and *Eriophorum vaginatum* (tussocks; similar to the methods of Mack et al. (2011)). *S. fuscum* moss appeared in

142 large mats. *Dicranum* moss appeared in small dense patches. All vegetative reference points were particularly

143 conspicuous in burned areas as they were elevated above the burned surface (Fig. 2). In the burned area, we

144 measured the distance from the soil surface to top of the living parts of the vegetative reference points, which we

145 assumed to indicate full survival in the fire event. We did not measure dead remnants of vegetative reference points,

146 because we expect that these may not represent the actual pre-fire vegetation height.

147
148 **Figure 2.** An example burn depth measurement from the surviving top of a *Dicranum spp.* moss patch (red arrow;
149 pink string) to the top of the soil (blue arrow) in a burned transect. Transect tape was used to measure distance
150 between the moss patches.
151
152   We measured the average height along a transect between two comparable reference points. At the highest

153   living point on each moss patch, or to the top of the corms at the base of a tussock, we inserted a nail (red arrow,

154   Fig. 2). We ran a taut piece of string between the two nails (Fig. A1). In between the edges of the moss patch or

155   tussock pair (Fig. A1), we took height measurements vertically from the string to the ground, which was soil in the

156   burned areas (blue arrow, Fig. 2) or a dense vegetative surface in the unburned areas (Fig. A2). In between the

157   starting and ending point measurements on the transect we recorded height every 25 centimeters (Figs. A2 and A3).

158   The starting and ending points were never greater than 50 centimeters from the nail. Latitude and longitude were

159   recorded at all transects with an accuracy of three meters (Fig. 1) for ground-truthing remotely sensed burn severity

160   categories.

161   One potential source of error is post-fire subsidence between the vegetative reference point pairs that may

162   bias the relative height of a vegetative marker above the surface (Jones et al., 2015). We minimized this potential

163   bias by maintaining transect lengths less than four meters, and predominantly one to two meters in burned areas.

164   We also visually assessed the area between each vegetative marker for signs of subsidence, including cracked soil or

165   large elevation differences, and chose not to sample these areas. Measuring from the top of one vegetative marker to

166   the top of another marker controlled for slopes and larger landscape elevation features because the string largely

167   mimicked the angle of the landscape.

168   We selected transects for height measurements opportunistically in the burned and unburned areas.

169   However, we tried to maximize spatial separation between transects and target visually identifiable areas of varying

170   burn severity. We corrected for spatial autocorrelation biases between transect averages in our statistical analyses

171   (see below). In unburned areas we maximized the number of transects measured for each vegetative reference point,

172   *Sphagnum* (n = 38), *Dicranum* (n = 40), and *Eriophorum* (n = 19).

173   Each burn depth measurement was associated with a dNBR value based on the 90 m pixel, the mean of

174   underlying 30 m pixels, containing its centroid. Burn depth measurements that came from the lowest third, middle

175   third, and upper third of dNBR values were considered to be in low severity/unburned, moderate severity, and high

176   severity areas, respectively, and a roughly even numbers of transects were sampled in each burn severity category

177   for *Sphagnum* (n = 56: high n = 20, mod n = 17, low/unburned n = 19), *Dicranum* (n = 54: high n = 18, mod n = 17,

178   low/unburned n = 19), and *Eriophorum* (n = 24: high n = 7, mod n = 11, low/unburned n = 6). Unburned patches of

179   tundra were sometimes included in low severity pixels within the burn scar, which is why these severity classes are

180   combined.

181   **2.4 Organic matter and carbon pool measurements**

182   We calculated the total ecosystem organic matter and carbon pool sizes in unburned areas surrounding the

183   fire scar. We took vegetation and soil samples together in cores using a hand drill and hollow metal drill bit that was

184   30 centimeters in length and six centimeters in diameter. Cores were extracted at three points (start, middle, and

185   end) along transects between like vegetative reference points. We selected four sites of less than half a hectare

186   surrounding areas where we took our unburned vegetative reference point height measurements. These sites were

187   selected opportunistically to ensure the presence of an appropriate number of each of the three vegetative reference

188   points. In each site, we extracted cores from three transects per vegetative reference point pair, which totaled 27 soil

189   cores per site. In one site we found only two tussock pairs, so our total number of samples was 105. We chose

190   unburned sites separated by at least one kilometer to control for heterogeneity in local soil and vegetation

191   characteristics.

192   We measured the height of the live vegetation layer and fibric soil horizons for each core. Vegetation

193   layers and soil horizons were identified visually by soil density, texture, color, and identifiable plant parts. Each

194   core was separated into vegetation and fibric soil layers that were homogenized, weighed, and subsampled in the

195   field, and subsequently stored frozen until analyzed. In the lab, each vegetation sample and approximately 15 grams

196   of each fibric sample were dried for 48 hours at 60 ℃ and weighed to determine soil water content. We used the

197   proportion of dry mass to wet mass to estimate the dry weight of the field sample, which was used to determine bulk

198   density (g dry mass cm^{-3}). Soil samples were combusted for five hours at 450 ℃ to determine organic matter

199   content and analyzed for percent carbon using an Elementar Vario Max CN analyzer at the Woodwell Climate

200   Research Center, Falmouth, MA. We assumed the dry mass of the vegetation layer was fully organic matter. Using

201   the average across all herbaceous plant organs, we assumed the carbon content of the vegetation layer was 43.04%

202   from Ma et al. (2018). To calculate organic matter and carbon pools (kg m^{-2}) for each organic soil sample, we

203   multiplied bulk density by the height of the layer and percent organic matter or percent carbon, respectively. These

204   values were normalized for each sample to the average depth of the vegetation layer, which was seven centimeters,

205   and 10 centimeters in the fibric horizon.

206   **2.5 Calculating final estimates**

207   We calculated organic matter combustion and carbon loss across the fire area using burn depth derived

208   from the moss reference points. We excluded estimates derived from tussock measurements, because our sample

209   size of tussock-based measurements was substantially lower than the moss vegetative reference points due to their

210   infrequent occurrence in our study area (Frost et al., 2020). Moreover, burn depth estimates from tussocks

211   correlated negatively with remotely sensed fire severity (Fig. A4).   This negative correlation with fire severity may

212   be attributable to mechanisms that are untestable with our sample size and study design, including altered burn

213   dynamics in close proximity to tussocks. Future work could clarify the mechanism behind this discrepancy.

214   Excluding tussock measurements required reassigning dNBR values evenly as before across only *Dicranum* (n = 54:

215   high n = 18, mod n = 18, low/unburned n = 18) and *Sphagnum* (n = 56: high n = 20, mod n = 18, low/unburned n =

216   18) reference points. The highest dNBR values in the low severity/unburned and moderate severity categories

217   became the threshold values for low severity/unburned to moderate severity and moderate severity to high severity

218   burn, respectively. We split the fire area, based on these thresholds, into the three categories for burn severity.

219   There were 13,001 hectares of low severity burn, potentially including unburned patches, 8,516 hectares of moderate

220   severity burn, and 32,637 hectares of high severity burn, which summed to 54,154 hectares of total fire area (Fig.

221   A5).

222   For final analysis of organic matter and carbon loss, we averaged the height of *Sphagnum* and *Dicranum*

223   reference points in the unburned areas to determine one height for each reference point, since their respective

224   heights were statistically different ($p < 0.001$). Burn depth was calculated at each transect in the burned areas by

225   subtracting the standard unburned height from the transect average height. We also averaged the dry organic matter

226   and carbon pool within the vegetative layer and fibric horizon separately across *Sphagnum* and *Dicranum* reference

227   points to determine one pool size for our sampling area. Average organic matter or carbon loss (kg m^{-2}) was

228   estimated as the product of the organic matter or carbon concentrations and depth of the vegetation and soil that

229   burned at each burn depth transect. Average loss at each transect was the sum of loss from each horizon (see Fig.

230   A6 for schematic of organic matter and carbon loss calculation per transect). For our final calculation of total dry

231   organic matter and carbon loss, we averaged the organic matter and carbon lost across transects for *Sphagnum* and

232   *Dicranum* reference points within each fire severity category. Over the landscape, total carbon or organic matter

233   released was calculated by multiplying average carbon or organic matter loss for a given burn severity category by

234   the total burned area for that category. Total carbon or organic matter released was then calculated as the sum from

235   all three burn severity categories.

236   **2.6 Radiocarbon**

237   We used radiocarbon dating to confirm our burn depth measurements by comparing the radiocarbon age of

238   *Sphagnum* macrofossils on the burned soil surface with the radiocarbon age of *Sphagnum* macrofossils at different

239   depths of the unburned soil profile, similar to the methods of Mack et al. (2011). In the field we extracted one

240   unburned core and three burned cores of the same dimensions as our primary soil cores, described above. We

241   extracted a one-centimeter thick subsample of the cores every five centimeters in depth and froze the samples in a

242   sealed plastic bag until lab analysis. To construct an age profile, we analyzed unburned cores at depths of five to 20

243   centimeters for radiocarbon age. We assumed that a depth of zero centimeters had carbon from the time of harvest

244   in 2019. In the burned cores, we analyzed the zero-centimeter depth (i.e., surface) for radiocarbon.

245   In the lab, we visually identified *Sphagnum* branches in each of the subsamples being tested and rinsed

246   them with deionized water. The branches were then dried for 48 hours at 60 ℃, and roughly five milligrams of dry

247   branch matter per sample was sent to the W.M. Keck Carbon Cycle Accelerator Mass Spectrometry Laboratory at

248   the University of California Irvine for the ^{14}C content and δ^{13}C. Results for ^{14}C analysis are reported as the fraction

249   modern, which is defined as the ratio of the sample's carbon isotope ratio to that of a standard (Reimer, 2004).

250   Fraction modern values are calibrated to calendar years using OxCal online 4.4.1 (Ramsey, 2009), with the

251   appropriate modern era bomb curve taken from Hua et al. (2013). Due to the shape of the bomb curve, there are at

252   least two possible calendar years in which the carbon in the sample was fixed. However, we did not use the oldest

253   age for unburned samples with multiple calendar ages because the age of these samples must increase with depth

254   (Walker et al., 2019, Mack et al., 2011), which is not supported when considering the oldest calendar ages.

255   Furthermore, we were confident the burned samples were from the younger age because they were from visually

256   shallow burn depths. We compared the calendar age of carbon at the burned soil surface to age by depth profile

257   taken from the unburned core.

258   **2.7 Radiative forcings model**

259   We created a temporally-explicit model of radiative forcings for gaseous and aerosol emissions of tundra

260   wildfires and used it to compute the radiative forcings per unit burned area. The radiative forcings model was

261   driven using the average amount of organic matter lost across fire-wide burn severity classes and vegetative

262   reference points. Computing the radiative forcing of gaseous and aerosol emissions has been done for boreal fires

263   (e.g., Huang et al. 2016, O'Halloran et al., 2012, Randerson et al., 2006), but has yet to be applied to tundra systems.

264   Our model included the long-lived GHG species CO_2, CH_4, and N_2O, as well as short-lived climate forcers,

265   tropospheric O_3, O_3 precursors, and aerosols. Ozone precursors include NO_x, non-methanogenic volatile organic

266   carbons (NMVOCs), and CO.

267   We first used emissions factors from Akagi et al. (2011) to calculate the mass of gaseous and aerosol

268   emissions from our estimated organic matter losses. Emissions factors have not been previously defined for tundra

269   burning. Given that boreal forest, whose definition for emission factors includes organic soils, peat, and woody

270   vegetation, is likely the closest ecosystem type in terms of fuel properties to tundra in Akagi et al. (2011), we

271   employed these emission factors. However, we note a possible overestimate of relative contribution from woody

272   vegetation emissions in these numbers due to the relative lack of woody vegetation on the tundra landscape.

273   Furthermore, concentrations of gasses released from combustion of the same biomass type vary based on the

274   measurement technique, such as from differences in chemical mixing in laboratory, airborne, and ground-based field

275   methods (Akagi et al., 2011). Since Akagi et al. (2011) provides estimates of each emissions factor based on a

276 combination of values from previous studies, the emissions factors may capture uncertainty associated with the

277 variable methods of these source studies.

278   Once we estimated the mass of each gaseous emission, we calculated the concentration of the gas

279 remaining in the atmosphere and its radiative forcing each year after the fire season by synthesizing existing models

280 and research on the lifetimes and radiative forcings of these gaseous emissions. Our calculations of radiative forcing

281 were dependent on the future ambient concentration of GHGs in the atmosphere. As a result, we calculated the

282 radiative forcings of gaseous emissions for three scenarios: historic, representative concentration pathway (RCP)

283 4.5, and RCP 8.5. The historic scenario assumes the ambient concentration of GHGs remains constant in the

284 atmosphere after the fire year. Future atmospheric concentrations for each RCP were taken from Meinshausen et al.

285 (2011). The radiative forcing for each gaseous emission per year was calculated separately and then summed across

286 forcing agent. Since O_3 precursors and aerosols had the most uncertain lifetimes and radiative forcings (Bond et al.,

287 2011, Quinn et al., 2008), we calculated the total radiative forcing of the emissions with and without them. A

288 flowchart of our general methodology for the entire radiative forcings calculation is presented in the appendix (Fig.

289 A7).

290 **2.8 Methane and Nitrous Oxide**

291   Our radiative forcing calculations for CH_4 and N_2O were based on Ward et al. (2012). For both gasses, we

292 assumed a pulse emission and calculated the concentration remaining in each year after the fires using a simple box

293 model with one outflow as shown in Eq. (3), where C_o is the initial pulse concentration of the gas, t is the number of

294 years after the fire event, and L is the lifetime of the gas. The initial pulse concentration of both gasses was

295 calculated by converting the mass emitted to a volume as a molar fraction of the atmosphere.

296 $$C = C_o e^{\frac{-t}{L}},$$ (3)

297 $$L = L_o \left(\frac{E}{E_t}\right)^{-0.05},$$ (4)

298

299   We used the atmospheric lifetimes for both gasses reported in Myhre et al. (2013). However, we calculated

300 a decreased lifetime of N_2O using Eq. (4) from Ward et al. (2012), as its ambient concentration changed in future

301 emissions scenarios, where L_o is the initial lifetime of N_2O from Myhre et al. (2013), E is the ambient concentration

302 of N_2O in the year the fires burned, and E_t is the ambient concentration of N_2O at each year after the fire event based

303 on the future emissions scenario (Meinshausen et al., 2011). We did not account for the effect of the changing

304 atmospheric concentration on the lifetime of N_2O due to the pulse emission itself. We then calculated the

305 perturbation concentrations of CH_4 and N_2O in the atmosphere each year after the fire event as the sum of the

306 remaining pulse emissions and the ambient concentrations and used Eqs. (5) and (6) from Ward et al. (2012) to

307 estimate the radiative forcing of both gasses. The radiative forcing of the gas at each year was RF, M was the

308 perturbation concentration of the gas whose radiative forcing was being calculated, and M_o and N_o were the ambient

309 concentrations of both gasses depending on which gas's radiative forcing was being calculated.

310 $$RF = 0.036\left(\sqrt{M} - \sqrt{M_o}\right) - [f(M,N_o) - f(M_o,N_o)], \tag{5}$$
311 $$f(M,N) = 0.47ln[1 + 2.01 \times 10^{-5}(MN)^{0.75} + 5.31 \times 10^{-15}M(MN)^{1.52}], \tag{6}$$
312
313 **2.9 Carbon Dioxide**

314 Carbon dioxide has a highly variable lifetime under different future emissions scenarios depending on the

315 strength of ocean and land sinks. To account for this variation, we used impulse response functions (IRFs) from

316 Joos et al. (2013), which represent the fraction of a pulse of CO_2 remaining in the atmosphere at each year after the

317 pulse for each scenario. For each year post-fire, we multiplied the relevant IRF function by the concentration of

318 CO_2 initially released to estimate the amount of CO_2 remaining in the atmosphere. Similar to N_2O and CH_4, the

319 initial concentration of CO_2 was calculated by converting the mass emitted to a volume as a molar fraction of the

320 atmosphere. The radiative forcing for CO_2 was calculated using Eq. (7) taken from Myhre et al. (1998), where C is

321 the perturbation concentration and C_o is the ambient concentration of the gas in each year.

322 $$RF = 5.35 \, ln\left(\frac{C_o + C}{C_o}\right), \tag{7}$$
323 **2.10 Tropospheric Ozone**

324 Tropospheric O_3 is created photochemically in the smoke plumes of wildfires by the combination of

325 sunlight and O_3 precursor gasses, and its creation can be expressed as a function of time and the amount of carbon

326 monoxide released (Jaffe and Wigder, 2012). We used data compiled in Jaffe and Widger (2012), who provided a

327 synthesis of O_3 and its relationship with CO for fire plumes sampled in the Arctic at various times after a fire to

328 calculate a mean plume lifetime and derive a linear relation between plume age and the ratio of O_3 to CO. Because

329 the average plume age sampled was five days, we assumed O_3 was created for five days after the fires. The

330 concentration of O_3 on each of those five days was calculated by multiplying the initial concentration of CO released

331 from the fires, calculated by converting the mass emitted to a volume as a molar fraction of the atmosphere, by the

332 ratio of O_3 to CO we estimated for that day. After five days, we assumed no more O_3 was created, and we

333 calculated the remaining amount of O_3 after day five using the box model approach from Eq. (3). The concentration

334 of O_3 on day five was C_o, and L was the lifetime of O_3 taken from Myhre et al. (2013). We converted the

335 concentration of O_3 to Dobson units (DUs) and converted from DUs to radiative forcing using a conversion factor

336 from Myhre et al. (2013) each day after the fire event. The radiative forcing in each year was the mean radiative

337 forcing of all the days within that year, although the annual forcing was negligible after the first year.

338 **2.11 Ozone Precursors and Aerosols**

339 We used a method based on global warming potential (GWP), similar to Huang et al. (2016), to calculate

340 the radiative forcing of the ozone precursors and the direct aerosol effect. GWP is defined as the ratio of the time-

341 integrated radiative forcing of a pulse emission of a gaseous species to the time-integrated radiative forcing of an

342 equivalent emission mass of CO_2 (Joos et al., 2013). GWP is typically calculated for 20- and 100-year time

343 horizons. Here, we use GWPs to determine the warming effect of the precursor and aerosol emissions relative to

344 CH_4 at the 20- and 100-year time horizons, as shown in Eq. (8). We derived the radiative forcings for ozone

345 precursors based on CH_4 because the radiative forcing of ozone precursors is through their effect on methane over

346 the long-term (Collins et al., 2013). To remain consistent with our methodology for ozone precursors, we derive the

347 radiative forcings for aerosols from CH_4 as well. Furthermore, the radiative forcing of CH_4 has the simplest

348 derivation in our model, so we assume it is the strongest continuous radiative forcing from which to build our

349 continuous model using GWPs.

350 $$R_t = \frac{GWP_{t,x} \times EF_x}{GWP_{t,CH_4} \times EF_{CH_4}}, \tag{8}$$

351 The emissions factor (EF) and GWP are defined for gaseous species x, and the GWP is defined at the time

352 horizon t. For CO and NMVOCs, we interpolate this relative warming effect (R_t) between year one and year 20 by

353 assuming it remains constant. To interpolate this effect between years 20 and 100, we mirror the shape of methane's

354 cumulative radiative forcing curve over that time interval. From this curve we calculated the difference between

355 methane's cumulative radiative forcing at years 20 and 100. We then calculated the fractional decrease of this

356 difference each year between years 20 and 100. We multiplied those fractional decreases by the difference in R_t at

357 years 20 and 100 for CO and NMVOCs to derive a relative warming effect for the precursors. Finally, we

358 multiplied R_t by methane's cumulative radiative forcing curve to estimate the cumulative radiative forcing for each

359 precursor every year after the fire event. We used the global GWPs for CO and NMVOCs from Myhre et al. (2013).

360 Since NO_x has a positive GWP at the 20-year time horizon and a negative GWP at the 100-year time

361 horizon, we chose not to mimic the shape of methane's radiative forcing curve when interpolating between the two

362 time points. Instead, we calculate an R_t value for NO_x at year one by scaling R_{20} in proportion to the change of

363   methane's cumulative radiative forcing from years one to 20. Then we interpolated between the R_t values in years

364   one, 20, and 100 using an exponential decay function of the form $ae^{-bx} + C$, whose coefficients were calculated

365   using the "nls" function in R (R Core Team 2020). We multiplied the R_t value for NO_x at each year by the

366   cumulative radiative forcing of CH_4 in that year to obtain a cumulative radiative forcing curve for NO_x. We use the

367   global GWP for NO_x from Myhre et al. (2013).

368   The radiative effect of aerosol emissions happens within a year of the fire event, as fire aerosols are

369   typically removed from the atmosphere via wet and dry deposition within a matter of weeks (Bond et al., 2011,

370   Quinn et al., 2008). We assumed that the cumulative radiative forcing of aerosols at any year after the fire event

371   would be constant and equal to the radiative forcing of aerosols in the year of the fire event. Therefore, to calculate

372   the cumulative radiative forcing from black and organic carbon direct effects in every year, we used R_{20} and

373   multiplied this value by the cumulative radiative forcing curve of CH_4 at year 20. Radiative forcings of black and

374   organic carbon were summed to report a single value for aerosols. We used the GWPs for black and organic carbon

375   estimated for open biomass burning including the cryosphere effect from Bond et al. (2011). To estimate the

376   indirect aerosol effect, we multiplied the radiative forcing of the direct effect of aerosols each year by the ratio of

377   indirect to all sky direct effect radiative forcing from wildfires defined in Ward et al. (2012).

378   **2.12 Statistical analyses**

379   All statistical analyses were completed in R (R Core Team 2020) using the nlme package (Pinheiro et al.,

380   2020). For the vegetative reference point heights, we used the nlme package function "gls" to fit a linear model

381   using the generalized least squares method with average burn depth and height above the dense vegetation layer

382   along the transect as the response variable in the burned and unburned areas respectively. Within the "gls" function,

383   both models were corrected for spatial autocorrelation between transect locations by choosing the model with the

384   lowest Akaike information criterion (AIC) score across five correlation structures, exponential, Gaussian, linear,

385   rational quadratic, and spherical, to be our final model. In burned areas, the model had vegetative reference point

386   nested within burn severity type, while in unburned areas, we only modeled the effect of vegetative reference point

387   type. The model with the lowest AIC score for both burned and unburned areas had a rational quadratic correlation

388   structure. To analyze differences in organic matter and carbon pools, height, and bulk density of the vegetation and

389   fibric soil layers we used the "lme" function, defined in the nlme package, to fit linear mixed effect models with the

390   restricted maximum likelihood method. These models had the soil or vegetation layer characteristic value for each

391   core as their response variable, vegetative reference point type as a fixed effect, and transect number nested in site as

392   random effects. Finally, we created linear fit models using the "gls" function with organic matter combusted and

393   carbon lost at each transect in the burned areas as response variables with the same structure as the burn depth

394   model. These models had the lowest AIC scores with a rational quadratic correlation structure. An analysis of

395   variance (ANOVA) was used to test for significant differences between groups for all of our models.

396   **3 Results**

397   We found that burn depth measurements were consistent with burn severity classification, and burn depth

398   increased with fire severity (Fig. 3). Based on a two-factor ANOVA with vegetative reference point nested within

399   burn severity, differences in average transect burn depth were significant ($p < 0.0001$) between burn severity

400   categories. The ranges of moderate severity burn depth measurements overlapped substantially with the high

401   severity and low severity/unburned measurements. Moderate severity groups also had the most evenly distributed

402   probability densities across burn depth. *Dicranum* measurements captured the shallowest and the deepest burn

403   depths (Fig. 3). Nevertheless, across both vegetative reference points, there was a clear stepwise increase in burn

404   depth across burn severity classifications.
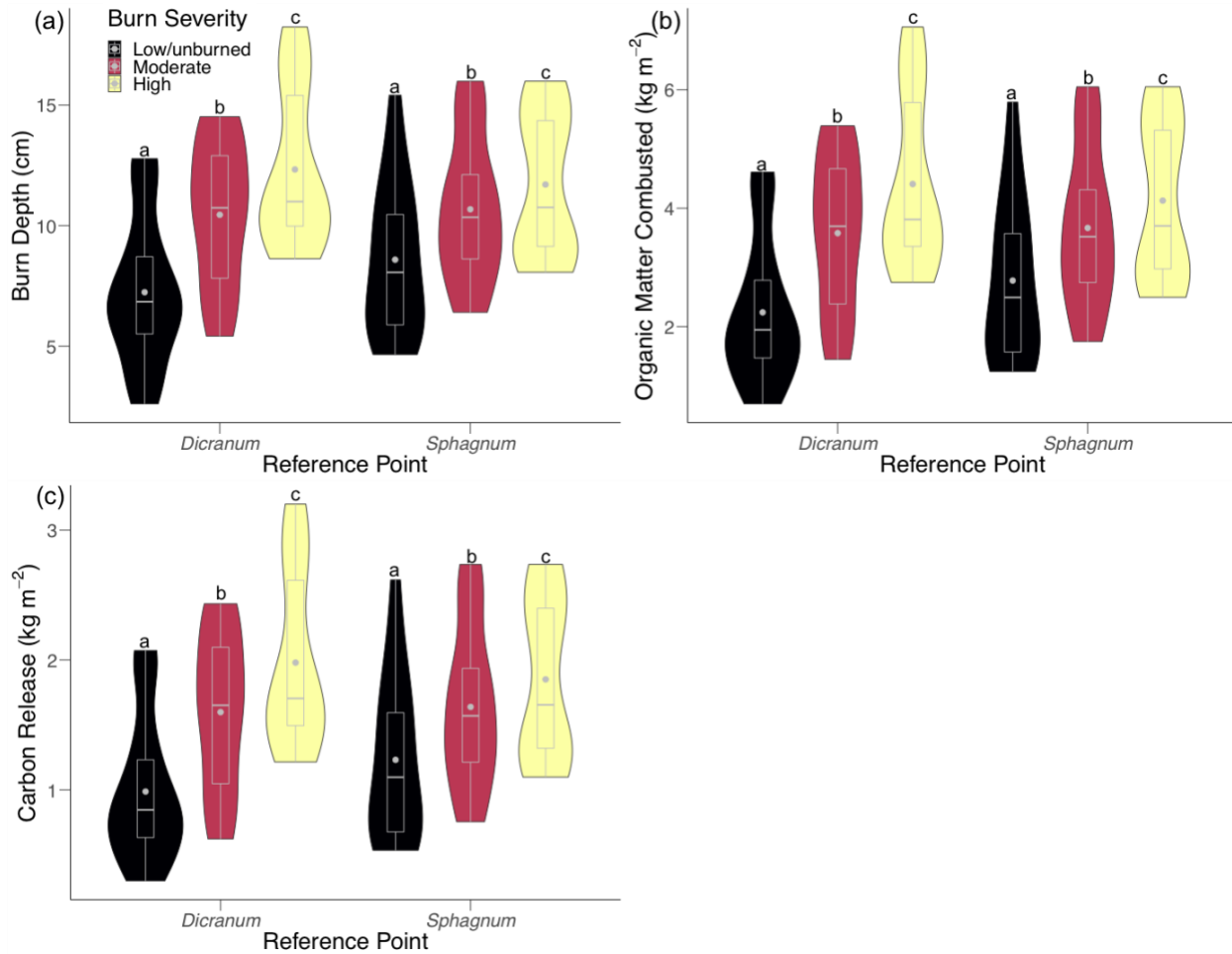
Figure 3. Distributions of average (a) burn depth, (b) organic matter combusted and (c) carbon released per unit burned area per transect within each reference point across burn severity levels. Boxes encompass the middle 50% of data, whiskers are the upper and lower quartiles, horizontal lines intersecting boxes show the median, and gray points are the mean. Letters indicate significantly different groups of data.

We found no significant differences between vegetative reference point types in terms of mean organic matter pool size, carbon pool size, height, or bulk density for either the live vegetation layer or fibric soil horizon extracted in our unburned cores ($0.3504 < p < 0.9558$). In the unburned areas, the fibric soil horizon (17.9 ± 0.63 cm) was nearly three times thicker than the vegetation layer (6.19 ± 0.60 cm) to the depth that our cores reached (~30 cm; Table 1), which is likely an underestimate of the soil organic layer depth, given that our cores only occasionally reached the mineral soil layer. However, there was larger variation in the vegetation layer ($1\sigma = 6.9$ cm) than fibric horizon ($1\sigma = 2.6$ cm) height. In most cases, the fire burned through the vegetation layer, but never completely through the fibric horizon (Fig. 3, Table 1). The fibric layer (to 24.1 cm average) had almost three times

420   greater organic matter and carbon pool sizes compared to the vegetation layer because of its higher bulk density and

421   height (Table 1).

422   **Table 1.** Bulk density, height, and carbon and organic matter percent and pool sizes of vegetation and fibric layers
423   measured in unburned soils averaged across reference points. Carbon and organic matter pool measurements are the
424   product of bulk density and their percent contents and are normalized to the height of the vegetation layer and 10
425   centimeters in the fibric layer. Sample size is 72, which is equally attributable to the two reference points. Error is
426   reported as the standard error of the mean (SEM).

Layer	Bulk Density (kg m^{-3})	Height (cm)	Percent Carbon (%)	Carbon Pool (kg m^{-2})	Percent Organic Matter (%)	Organic Matter Pool (kg m^{-2})
Vegetation	26.7 ± 1.4	6.19 ± 0.60	43.04*	0.712 ± 0.037	100*	1.65 ± 0.09
Fibric	54.6 ± 5.0	17.9 ± 0.63	39.41 ± 0.56	2.07 ± 0.16	88.12 ± 1.17	4.48 ± 0.30

427   *Based on assumption

428
429   Carbon and dry organic matter loss estimates similarly increased with burn severity (Fig. 3, Table 2).

430   Based on a two-factor ANOVA with vegetative reference point nested in burn severity, average organic matter and

431   carbon loss differed between burn severity categories (carbon loss: $p < 0.0001$; organic matter loss: $p < 0.0001$) (Fig.

432   3). Similar to burn depth distributions, the moderate severity range overlapped with the high severity and low

433   severity/unburned distributions (Fig. 3).

434   **Table 2.** Carbon and organic matter loss averaged within each burn severity category across reference point, and
435   total carbon and organic mass loss over each burn severity category area. Total loss per burn severity category is
436   summed to calculate total loss over the total fire area by burn severity classification. Error is reported as SEM,
437   except for total loss over the fire area which is reported as the sum of errors.

438

Severity	Sample Size	Area (hectares)	Carbon Loss		Dry Organic Matter Loss	
			Average (kg m^{-2})	Total (Tg)	Average (kg m^{-2})	Total (Tg)
Low/unburned	36	13,001	1.11 ± 0.10	0.144 ± 0.013	2.51 ± 0.22	0.326 ± 0.029
Moderate	36	8,516	1.62 ± 0.10	0.138 ± 0.009	3.62 ± 0.22	0.309 ± 0.019
High	38	32,637	1.93 ± 0.12	0.629 ± 0.039	4.29 ± 0.23	1.40 ± 0.08
Total	158	54,154		0.911 ± 0.039 (Tg)		2.04 ± 0.09 (Tg)

439
440   The 2015 fires burned a total of 54,154 hectares in the YKD. The distribution of dNBR values for our

441   focal fires in the YKD was intermediate compared to dNBR values from all tundra fires and on the low side but

442   within the range of dNBR values for all boreal fires in Alaska between 1989 and 2019 (Fig. A8). Roughly 60% of

443   the burned area was classified as high severity, while moderate severity and low severity/unburned accounted for

444   about 16% and 24% of the burned area, respectively (Table 2). As a result, total organic matter and carbon loss

445   within the high severity burn classification was over three times greater than the other two burn severity categories.

446   Although moderate severity occupied less fire area than the low severity/unburned, it contained roughly equal total

447   organic matter and carbon loss to the low severity/unburned areas due to about 50% higher organic matter and

448 carbon losses per unit area on average. However, it should be noted that losses from low severity/unburned areas

449 are likely overestimates, given the inclusion of unburned areas within regions of low severity burn. Summing

450 carbon loss and dry organic matter loss over the area of each burn severity category yielded a total loss of 2.04 ±

451 0.09 Tg of dry organic matter and 0.911 ± 0.039 Tg of carbon. This magnitude of total loss corresponded to an

452 average 3.76 kg m^{-2} of organic matter and 1.68 kg m^{-2} of carbon loss across the fire area.

453   The age of carbon increased by ~50 years from 5 to 20 cm in depth in the unburned area. Surface samples

454 from burned soils in a low severity/unburned area were dated to 2009, indicating a burn depth of about 5 cm or less,

455 which is within the range of our low severity/unburned burn depth measurements (Table 3). The rate of change in

456 carbon age between 0 and 5 cm was 2.4 yr cm^{-1}; for the 15 to 20 cm interval, it was 3.6 yr cm^{-1}. Because none of

457 our burn depth measurements exceeded 20 cm, all carbon released from the fires was likely relatively new carbon,

458 younger than 64 years of age. Our average burn depth of 10.3 cm across burn severity and reference point indicated

459 an average age of about 23 years for carbon released.

460 **Table 3.** The fraction of the modern standard and calibrated calendar age for each radiocarbon sample. Calendar
461 ages are the intercepts for the fraction modern value with the calibration curve. We do not consider the oldest
462 calendar ages.

Burn Status	Depth (cm)	Fraction Modern	Calendar Ages CE
Burned	0	1.0486 ± 0.0020	1957, 2009
Burned	0	1.0493 ± 0.0024	1957, 2009
Burned	0	1.0403 ± 0.0018	1957, 2008, 2009
Unburned	5	1.0625 ± 0.0020	1957, 2007, 2008, 2009
Unburned	10	1.1198 ± 0.0023	1958, 1996
Unburned	15	1.4603 ± 0.0024	1963, 1974
Unburned	20	1.0124 ± 0.0017	1956

463
464   The radiative forcing for gaseous and aerosol emissions from the 2015 fire season was positive for 80 years

465 post-fire according to our model, regardless of the future atmospheric gas concentration scenario (Fig. 4a).

466 However, the magnitude of the fire emissions' radiative forcings decreased with increasing ambient atmospheric gas

467 concentrations, with RCP 8.5 having the lowest radiative forcing at 80 years post-fire (Fig. 4a). Given the lack of

468 qualitative difference across future scenarios, below we present results for the RCP 4.5 scenario only (Table 4, Fig.

469 4b). Nitrogen oxides were the only gas with a negative radiative forcing at the 80-year cumulative mean. However,

470 they had a positive radiative forcing at the 20-year time horizon (Table 4). The only other negative radiative forcing

471 came from the indirect effect of aerosols that completely counterbalanced the positive radiative forcing from other

472 gaseous emissions in the first year, but the magnitude of this effect in terms of cumulative integrated forcing

473 diminished rapidly after the first decade (Fig. 4b). CO_2 produced the highest radiative forcing through 80 years

474 (Table 4, Fig. 4b). Nitrous oxide sustained its positive radiative forcing; however, the radiative forcing was of

475 intermediate magnitude with respect to all gaseous emissions. In contrast, ozone and carbon monoxide exhibited

476 high radiative forcings, but the magnitude of these diminished rapidly with respect to carbon dioxide. Likewise, the

477 effect of the other ozone precursors, aerosols, and methane decreased relatively rapidly (Table 4). Overall, 20-years

478 post-fire, the effect of ozone precursors increased the total radiative forcing by roughly 11%. However, this percent

479 increase drops to 5% after 80 years, and the ozone precursors and aerosols show little effect on the percent reduction

480 of the total radiative forcing between 20- and 80-years post fire. Therefore, the positive radiative forcing is

481 sustained by long-lived gaseous emissions, especially carbon dioxide.
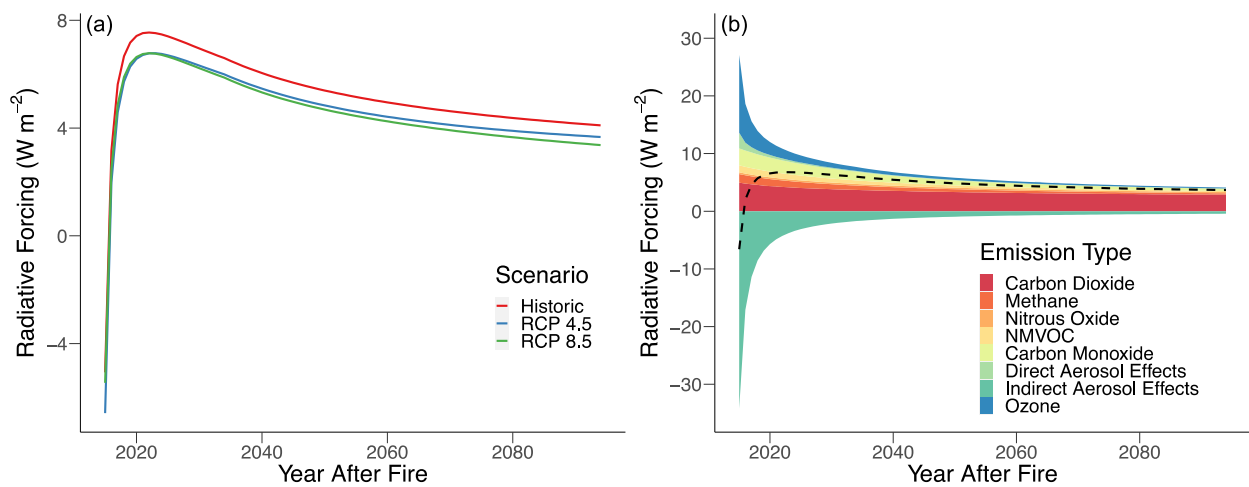
482
483 **Figure 4.** (a) Total cumulative mean radiative forcing of gaseous emissions for three future atmospheric gas
484 concentration scenarios, and (b) cumulative mean radiative forcing of different emissions (dashed line is net forcing)
485 under the RCP 4.5 future scenario over 80 years post-fire from the YKD 2015 fire season.

486
487 **Table 4.** Cumulative mean radiative forcing at 20- and 80- year time horizons post-fire for different gaseous and
488 aerosol emissions from the 2015 fire season under the RCP 4.5 future scenario. Percent reduction refers to the loss in
489 radiative forcing when considering an 80-year time horizon compared to 20 years.

	Radiative Forcing (W m^{-2})										
Time Horizon	CO_2	CH_4	N_2O	O_3	NMVOC	CO	NO_x	Indirect Aerosol Effects	Direct Aerosol Effects	Total with Ozone Precursors and Aerosols	Total without Ozone Precursors and Aerosols
20 years	3.69	0.76	0.28	0.67	0.62	1.51	0.03	-1.71	0.14	5.99	5.41
80 years	2.87	0.24	0.22	0.17	0.19	0.40	-0.01	-0.43	0.03	3.67	3.49
Percent Reduction (%)	22	68	21	75	69	74	133	75	79	39	35

490
491 **4 Discussion**

492 Here we describe a tundra wildfire season that combusted significant amounts of carbon and had a positive

493 warming effect on the atmosphere due to its gaseous and aerosol emissions over an 80-year time horizon. Our

494   findings suggest that increasingly frequent tundra fire regimes are an under-studied source of global GHG

495   emissions. The 2015 fire season in the YKD represents a large efflux of carbon from a wetland tundra ecosystem,

496   generally not considered to be highly vulnerable to fires. In total, we estimate that about 0.911 Tg of carbon was

497   released from 54,154 hectares of burned area in the YKD. This fire area is roughly three times the 17,000 hectares

498   of tundra area burned on average annually between the years 2001 and 2018 in Alaska, but it only accounts for a

499   little more than half of the 83,000 hectares of Alaskan tundra that burned in the year 2015 (Scholten et al., 2021).

500   Over the same time frame, the 2015 fire season was the largest to burn in the YKD, with the majority of years

501   burning less than 10,000 hectares (Scholten et al., 2021). Total carbon loss was driven by a similar per unit area

502   carbon emission rate as the 2007 Anaktuvuk River fire (Mack et al., 2011), which was roughly twice the size of the

503   fire season reported here and burned predominately moderate to high severity in a tussock tundra ecosystem (Jones

504   et al., 2009). While the current status of tundra ecosystems as a sink or source of carbon remains uncertain, the 2015

505   YKD fire season alone released about a tenth of the carbon sequestered annually from tundra sink estimates

506   (Virkkala et al., 2021). If tundra ecosystems become a source of carbon to the atmosphere under warming,

507   emissions from tundra wildfires may further exacerbate this positive feedback to warming due to a changing balance

508   between respiration and productivity (Natali et al., 2019, Belshe et al., 2013). Note that we did not account for post-

509   fire effects on net ecosystem exchange of CO_2, which tend to be sources to the atmosphere with greater fire severity

510   due to continued soil respiration until sufficient vegetation recovers (Rocha and Shaver 2011a).

511   The tundra fires in the YKD and at Anaktuvuk River both lost roughly 1.7 to 2.0 kg m^{-2} of carbon (Mack et

512   al., 2011). Carbon loss per area from these tundra wildfires is within the range of total above- and belowground

513   carbon loss from boreal wildfires, approximately 0.5 to 4 kg m^{-2} (Walker et al., 2020a; Walker et al., 2018b; Rogers

514   et al., 2014), and close in value to the median wildfire loss of carbon, 2.54 kg m^{-2}, across all land cover types in

515   Alaska between 2001 and 2012 (Veraverbeke et al., 2015b). Despite the additional combustion of overstory

516   vegetation in forests, carbon loss in both tundra and boreal systems comes primarily from belowground organic

517   matter (Walker et al., 2020a; Walker et al., 2018b; Rogers et al., 2014). Compared to remote sensing-derived

518   estimates of combustion, our per unit area *in situ* measurements are on the low end but comparable to large-scale

519   means across Alaska between 2001 and 2018 (Fig. A9). However, more representative field measurements in tundra

520   fires are needed to validate remotely sensed combustion measurements, as the currently available gridded products

521   (Potter et al. 2022; Scholten et al. 2021; Veraverbeke et al. 2017a; Veraverbeke et al., 2015a) are driven entirely by

522 measurements in boreal forests. Although data from the Anaktuvuk River and YKD fires shows carbon loss per unit

523 area can be similar between boreal and tundra wildfires, information on carbon emissions from tundra wildfires is

524 substantially more limited than boreal forest studies (He et al., 2021; Veraverbeke et al., 2021).

525 Given a fire return interval in the YKD of over around 200 years (Sae-Lim, 2019), fires there likely do not

526 burn through all the carbon accumulated since the last fire. However, tundra fires may initiate post-fire successional

527 trajectories, such as increased shrub cover, that may promote shorter fire return intervals (Hu et al., 2015; Rocha et

528 al., 2012). Shorter fire return intervals, in turn, gradually deplete the available soil carbon stocks. For example, He

529 et al. (2021) showed current tundra areas with frequent fire have relatively shallow soil organic layers. Moreover,

530 our radiocarbon data show that as fires burn deeper into the tundra, they release older carbon more rapidly because

531 the density of carbon by age increases. Coupling these burn-prone successional trajectories with projected increases

532 in tundra wildfire occurrence over the next century due to more frequent hot and dry conditions (Hu et al., 2015;

533 Rocha et al., 2012; Joly et al., 2012; Hu et al., 2010), as well as increases in lightning (Chen et al., 2021; Bieniek et

534 al., 2020; Veraverbeke et al., 2017b), tundra wildfires may begin to burn carbon of an older age than the historic fire

535 return interval. In this case, some tundra regions may transition into fire-driven carbon sources, similar to what has

536 been observed in North American boreal forests (Walker et al., 2019).

537 Immediate combustion is not the only impact wildfires have on tundra carbon stocks, nor do measures of

538 carbon loss fully describe the effect of wildfire emissions on the climate. Fires drive higher soil temperatures and

539 deeper active layer depths that can persist over multiple decades after fire (He et al., 2021; Hu et al., 2015; Rocha et

540 al., 2012), which is caused by the loss of insulating vegetation and upper soil layers from combustion (Rocha and

541 Shaver, 2011b). Higher soil temperatures and deeper active layer depths may catalyze permafrost degradation and

542 thermokarst development (Jones et al., 2015) that accelerates the effects of climate warming on tundra ecosystems.

543 Tundra fires also emit multiple gaseous and aerosol species, which have a net positive radiative forcing for at least

544 80 years post-fire. Hence, even if all of the carbon lost from fire in a tundra ecosystem were to be sequestered again

545 over time through increased photosynthesis, the long-term radiative impact of gaseous and aerosol emissions would

546 still generate atmospheric warming and thus positive climate feedbacks, which are amplified by the post-fire

547 permafrost thaw and degradation not accounted for in this study.

548 This positive radiative forcing is driven by sustained radiative forcings from long-lived GHGs, as well as

549 significant contributions from short-lived climate forcers (SCLFs) such as ozone, NMVOCs, and CO. Carbon

550 dioxide has the highest radiative forcing at both short and long time horizons because it is emitted in the highest

551 quantity (Akagi et al., 2011) and its concentration decreases relatively slowly over time, especially in the RCP 4.5

552 and 8.5 scenarios (Joos et al., 2013). Aerosols and NO_x are SCLFs with both positive and negative radiative

553 forcings due to distinct mechanisms for affecting the Earth's radiative balance. Aerosols exert a direct radiative

554 forcing by reflecting or absorbing sunlight in the atmosphere and when deposited on high-albedo surfaces, mainly

555 snow and ice (Bond et al., 2011). Although black carbon aerosols have a positive direct radiative forcing effect and

556 organic carbon aerosols have a negative direct radiative forcing effect, the magnitude of black carbon's radiative

557 forcing far exceeds that from organic carbon (Myhre et al., 2013) (note these are combined in our representation).

558 Indirectly, aerosols serve as the nuclei for cloud formation, which increases the Earth's albedo and exerts a negative

559 radiative forcing (Ward et al., 2012). Nitrogen oxides have a near-term positive radiative forcing because they act in

560 concert with NMVOCs and CO to increase ozone concentrations, yet they have a long-term negative radiative

561 forcing because they decrease the lifetime of CH_4 (Collins et al., 2013).

562   We include a total radiative forcing with and without aerosols and ozone precursors, CO, NMVOCs, and

563 NO_x. The radiative forcing of these ozone precursors and aerosols is uncertain within current literature, especially

564 when originating in the Arctic, because of their short atmospheric lifetimes and dependence on regional transport

565 patterns (Bond et al., 2011, Quinn et al., 2008). However, the long-term cumulative radiative effect of these gaseous

566 emissions is relatively minimal in comparison to the long-lived GHGs and ozone, and both estimates of total

567 radiative forcing are of the same order of magnitude as previous estimates of the radiative forcing of gaseous

568 emissions from boreal forest fires (Huang et al., 2016; O'Halloran et al., 2012).

569   We found that as the predicted concentration of future emissions increases across RCP scenarios

570 (Meinshausen et al., 2011), the net radiative forcing of gaseous and aerosol emissions from the fires decreases

571 slightly. Although counterintuitive, this result is due to the dependency of the radiative forcing equations for long-

572 lived GHGs, namely CO_2, CH_4, and N_2O, on the ambient concentration of a gas. In more extreme future climate

573 scenarios, the atmosphere generally has higher concentrations of these GHGs, meaning the additional quantity of gas

574 emitted by fire has a more diluted effect. This effect is largely counter balanced by the fact that land and ocean CO_2

575 sink capacities are diminished in more extreme future climate scenarios, leading to longer atmospheric CO_2 lifetimes

576 (Fig. A10). The net result is that tundra wildfires have a relatively similar positive radiative forcing under all future

577 emissions scenarios.

578   While the positive radiative forcing due to gaseous emissions we calculate for the 2015 YKD fire season is

579   within the range of previously calculated radiative forcings for gaseous emissions from boreal wildfires (e.g., Huang

580   et al., 2016, Randerson et al., 2006), boreal forests also have significant multi decadal post-fire albedo changes due

581   predominantly to the combustion of overstory trees that expose snow in the fall, winter, and spring (Lyons et al.,

582   2008). Randerson et al. (2006) and O'Halloran et al. (2012) show that the negative radiative forcing of these albedo

583   changes can exceed the positive radiative forcing of gaseous emissions and generate a net cooling effect for boreal

584   forest fires over long time horizons in specific locations. It should be noted, however, that (i) the net cooling or

585   warming is heavily dependent on combustion levels, pre-fire canopy composition, and time horizon; (ii) fire-induced

586   albedo forcings predominantly impact the regional climate (Rogers et al., 2013), as opposed to globally-mixed

587   GHGs; and (iii) this cooling impact is expected to diminish with future climate change due to decreases in spring

588   snow cover (Potter et al., 2020).

589   In contrast, tundra ecosystems lack an overstory, and hence fires generate relatively short-lived decreases in

590   albedo (Rocha et al., 2012, French et al., 2016). These albedo changes are only caused by char and the exposed soil

591   surface in the summer because tundra vegetation rarely exists above the snow layer (Mack et al., 2011). As a result,

592   within four years after the Anaktuvuk River fire, low post-fire surface albedo recovered to its pre-fire reflectance as

593   the vegetation grew over the charred soil surface (French et al., 2016; Rocha and Shaver, 2011b). The decreased

594   surface reflectance contributes to increases in soil temperature and thaw depth after fire (Rocha and Shaver 2011b).

595   Therefore, the positive radiative forcing caused by tundra wildfire gaseous and aerosol emissions is not offset by

596   post-fire albedo changes as seen in boreal forest fires. From 2001 to 2018 about 0.5 Mha of boreal forest burned on

597   average yearly compared to a yearly average of 0.017 Mha of tundra in Alaska (Scholten et al., 2021). Given

598   potentially comparable per area emissions from boreal and tundra fires, boreal fires still release more carbon

599   globally. However, the predicted increase in frequency of tundra wildfires, their lack of cooling from post-fire

600   albedo, and their contribution to increased permafrost thaw highlights their importance to climate change processes.

601   For the purpose of calculating the radiative forcing of wildfires in future research, we make our

602   computational code available on Github (see Code and Data Availability section). Our workflow is applicable to

603   wildfires in other arctic-boreal ecosystems, and it could be applied to any ecosystem globally with the adjustment of

604   emissions factors for the specific material burning (Akagi et al., 2011) and global warming potentials for SCLFs

605   based on the geographic region of the wildfire (Myhre et al., 2013). As a result, our method of calculating the

606 radiative forcing of wildfires can be used for studies across multiple regions with the appropriate parameters, which

607 can advance a more complete understanding of the effects of wildfires on the climate.

608   Future work could clarify some of the uncertainties that were not explicitly analyzed in our final estimates

609 of carbon loss and radiative forcing. We did not account for combustion of aboveground tall woody vegetation in

610 our estimates of carbon loss from the YKD fires. Although woody biomass is relatively sparse on the YKD

611 landscape, it represents an additional source of carbon from combustion (for boreal forest fires, see Walker et al.,

612 2020c). Despite the lack of difference we found between soil and vegetation matter characteristics across vegetative

613 reference point groups, there could have been variation in these characteristics outside of the primarily peat plateau

614 areas that we sampled. Burn depth estimated between *Dicranum* reference points was more variable (although not

615 significantly different) than burn depth estimated between *Sphagnum* reference points. This variation could indicate

616 more variable burn dynamics around *Dicranum* or better efficacy of *Dicranum* for measuring extreme burn depths,

617 which highlights the potential bias introduced by choosing specific combustion markers. Likewise, we eliminated

618 tussock measurements from our final analysis because they were relatively scarce on the landscape and yielded

619 inconsistent results, perhaps due to burn dynamics around tussocks that remain obscure using our combustion

620 measurement method. Minimizing potential bias by identifying combustion markers and soil characteristics for

621 different land cover types at a higher resolution within a fire, similar to how different combustion markers are used

622 regionally (Walker et al., 2020c; Mack et al., 2011; Boby et al., 2010) would further improve estimates of carbon

623 loss following wildfire in tundra systems.

624   Our assignment of low, moderate, and high severity was based on our particular collection of field

625 measurements and therefore may not translate well to other fire complexes. While dNBR is widely used to assess

626 fire severity, its accuracy in high latitude tundra systems may be diminished by environmental and methodological

627 factors, such as the timing of image selection and rapid post-fire greening (Chen et al., 2020a, Loboda et al., 2013).

628 Other remotely sensed products have shown promise in tundra (e.g., Chen et al., 2020b), but the applicability of

629 these results to other tundra systems remains to be explored. Within low severity areas, there were likely patches of

630 unburned tundra, potentially leading us to overestimate organic matter and carbon loss measurements. We also used

631 a relatively simple method for extrapolating emissions based on fire severity. More involved techniques such as

632 relating mechanism-based geospatial predictors to field plots using statistical techniques and machine learning,

633 which has been employed for boreal forests in Alaska and Canada (Dieleman et al., 2020; Walker et al., 2018b;

634   Veraverbeke et al., 2015b; Rogers et al., 2014), would likely yield more robust estimates for regional emissions. In

635   this context, we strongly recommend increasing the number of tundra fire carbon emission observations in different

636   regions to facilitate synthesis and biome-wide modeling, as has been done for boreal forests (Walker et al., 2020c;

637   Walker et al., 2020b; Walker et al., 2020a).

638   Our radiative forcings model uses data and algorithms from multiple previous studies, including for

639   emissions factors (Akagi et al., 2011), RCP scenarios (Meinshausen et al,. 2011), GWPs (Myhre et al., 2013), ozone

640   and CO concentration ratios (Jaffe and Widger, 2012), and aerosol direct and indirect effects (Ward et al., 2012), all

641   of which may not be geographically, biologically, or temporally specific to the YKD fires. These factors are also

642   known to be variable depending on fuel types, fire severity and lifetime, and atmospheric dynamics at the time of

643   and following fire (e.g., Wiggins et al., 2016; Jaffe and Widger, 2012; Chen et al., 2009). Since emissions factors

644   for tundra burning were not available, we used emissions factors for burning boreal vegetation. Using boreal

645   emissions factors may overestimate emissions from woody vegetation in tundra and thereby increase the mass of

646   certain gasses released. Future research could also integrate the range of variation associated with emission factors

647   to quantify the uncertainty they introduce into radiative forcing estimates. Furthermore, our model does not include

648   the potential mitigating or exacerbating effects of post-fire ecosystem changes on gas concentrations, such as

649   changes in post-fire vegetation (Frost et al., 2020; Zhou et al., 2019; Barrett et al., 2012), increased soil respiration

650   (Rocha and Shaver, 2011a), and increased active layer depths and permafrost degradation (Holloway et al., 2020;

651   Jafarov et al., 2013; Rocha et al., 2012). With reparameterizations specific to individual fires, our model could be

652   made more accurate for future work.

653   **5 Conclusions**

654   To our knowledge, our study is the first to account for both carbon loss and radiative forcing from tundra

655   wildfires. We develop a method that pairs *in situ* measurements of combustion levels from local pre-fire reference

656   points with remotely sensed burn severity data to scale organic matter and carbon loss to the entire fire area. Our

657   estimate of the radiative forcing of gaseous and aerosol emissions from the fire event suggests that tundra wildfires

658   positively reinforce climate warming; however, the role of post-fire vegetative regeneration in mitigating these

659   carbon emissions remains unknown. Our results stress the importance of considering tundra wildfires in assessing

660   climate feedbacks and the need for future research that more explicitly discerns the warming effect of fires across

661   the tundra biome.

662

663

664

665

666

667

668

669

670

671

672

673

674

675

676

677

678

679

680

681

682

683

684

685

686

687

688

689

 Appendix A
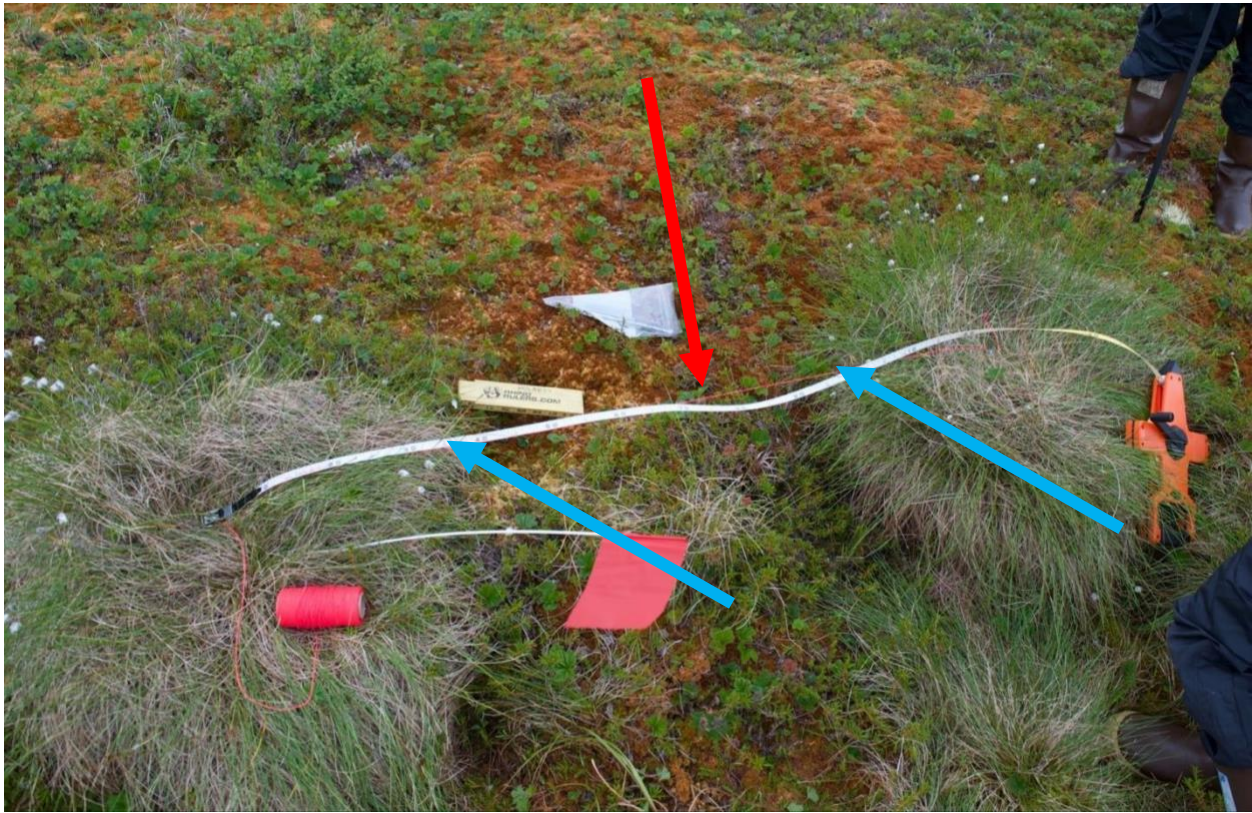
691
692 **Figure A1.** Height measurement of *Eriophorum vaginatum* in an unburned area from the taut string (red arrow) to
693 the dense vegetation layer between the starting and ending points (blue arrows) at the edge of each tussock patch.
694

695
696 **Figure A2.** Measurement from the taut string to the dense vegetative layer (red arrow) in an unburned area every 25
697 centimeters (blue arrow).
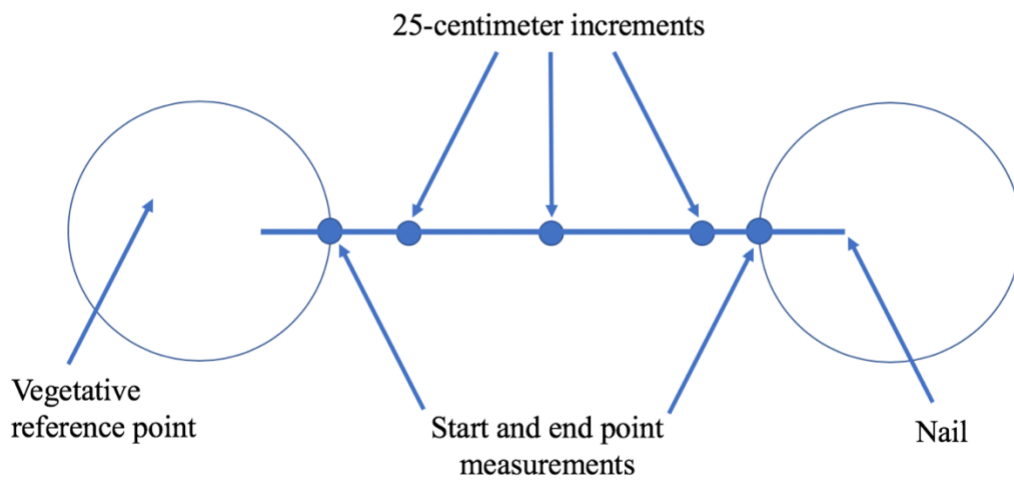
698
699 **Figure A3.** A schematic of the height measurements made along a transect between two vegetative reference points.
700
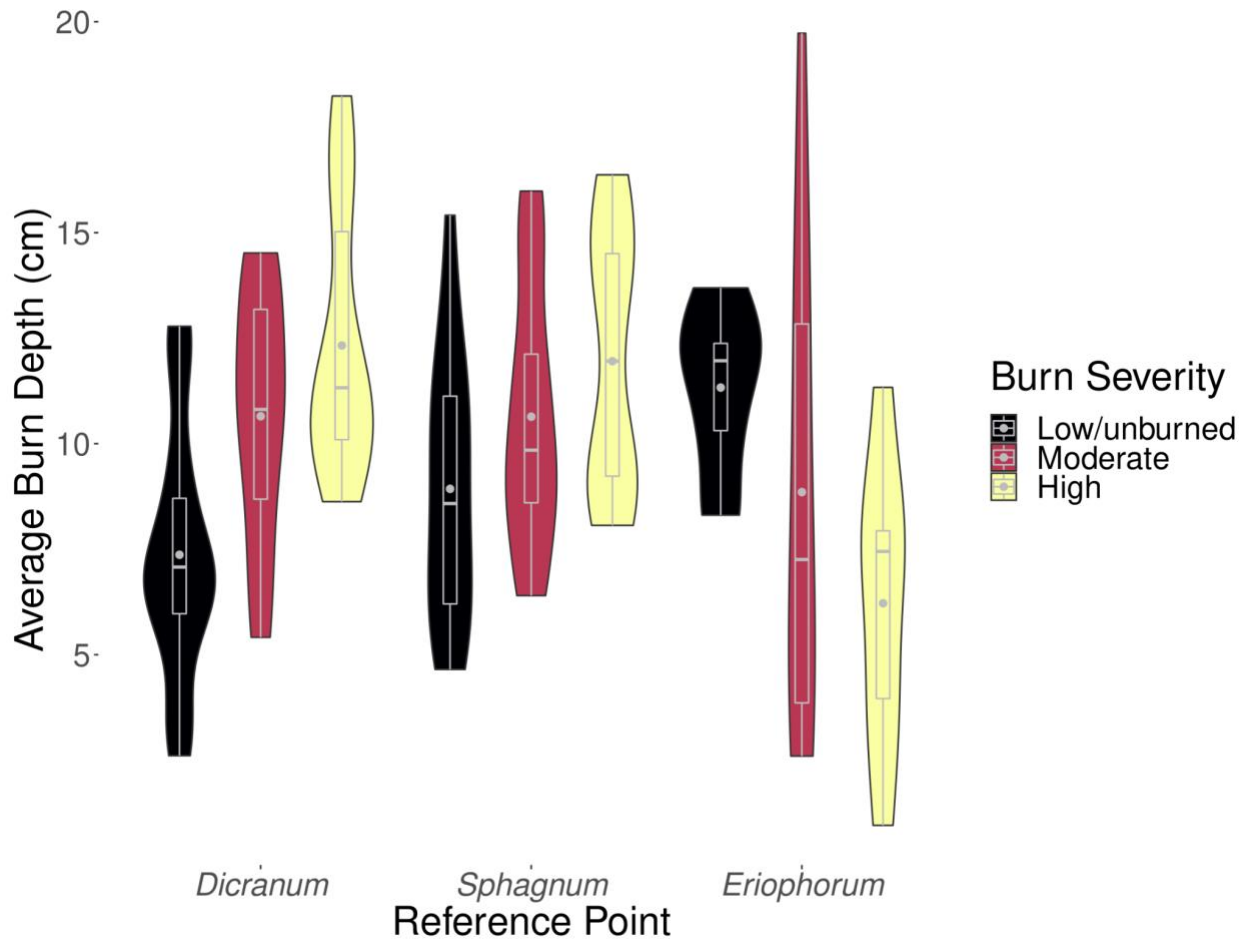
701
702 **Figure A4.** The distributions of average burn depth per transect within each reference point (including *Eriophorum*
703 *vaginatum*) across burn severity. Boxes encompass the middle 50% of data, whiskers are the upper and lower
704 quartiles, horizontal lines intersecting boxes show the median, and gray points are the mean.
705
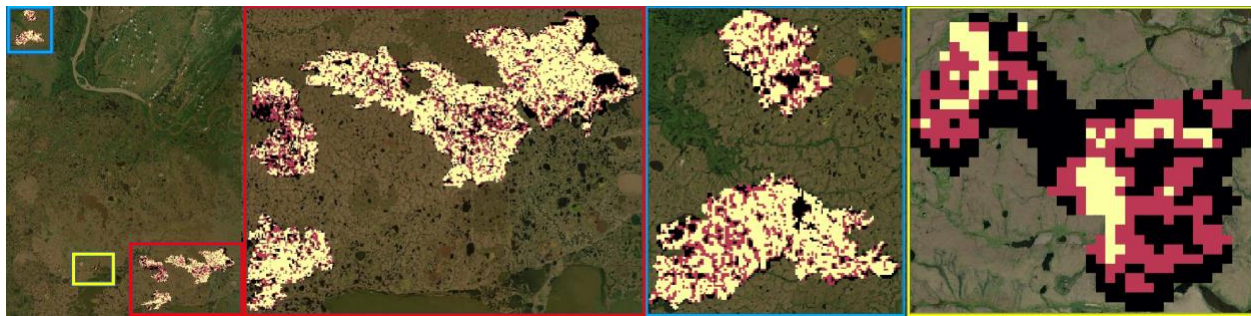
706

707 **Figure A5.** Fire severity across the YKD 2015 fire area categorized using dNBR values into low severity/unburned
708 (black), moderate severity (red), and high severity (yellow) categories. The panels show the total fire area (far left),
709 then close ups of the southeastern (red), northwestern (blue), and south-central (yellow) fire scars, respectively.
710 Basemap sources: Esri, DigitalGlobe, GeoEye, i-cubed, USDA FSA, USGS, AEX, Getmapping, Aerogrid, IGN,
711 IGP, swisstopo, and the GIS User Community.
712

713
714
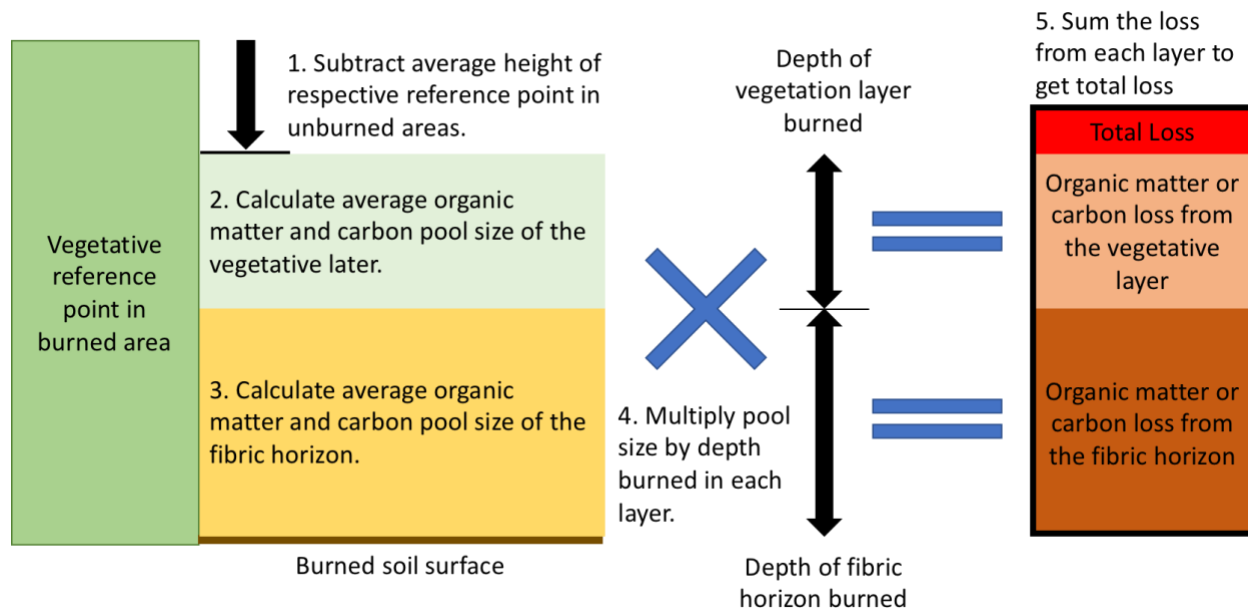
715
716 **Figure A6.** A schematic of organic matter and carbon loss calculations at a single transect in the burned area.
717
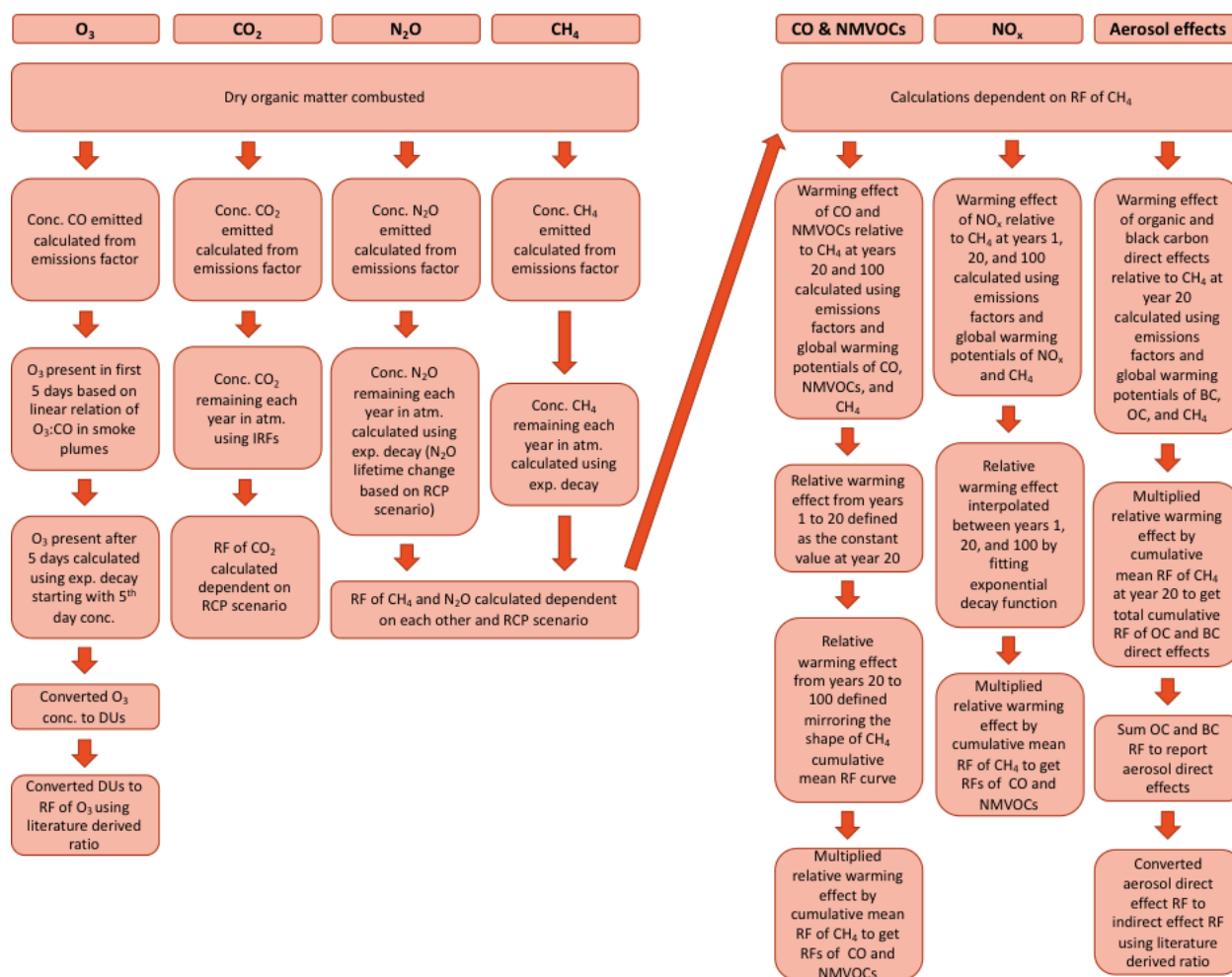
718

719 **Figure A7.** Flowchart of the methodology for the calculation of the radiative forcings of gaseous emissions from
720 biomass combustion generally applicable to any biome with adjustment of biome-specific parameters.
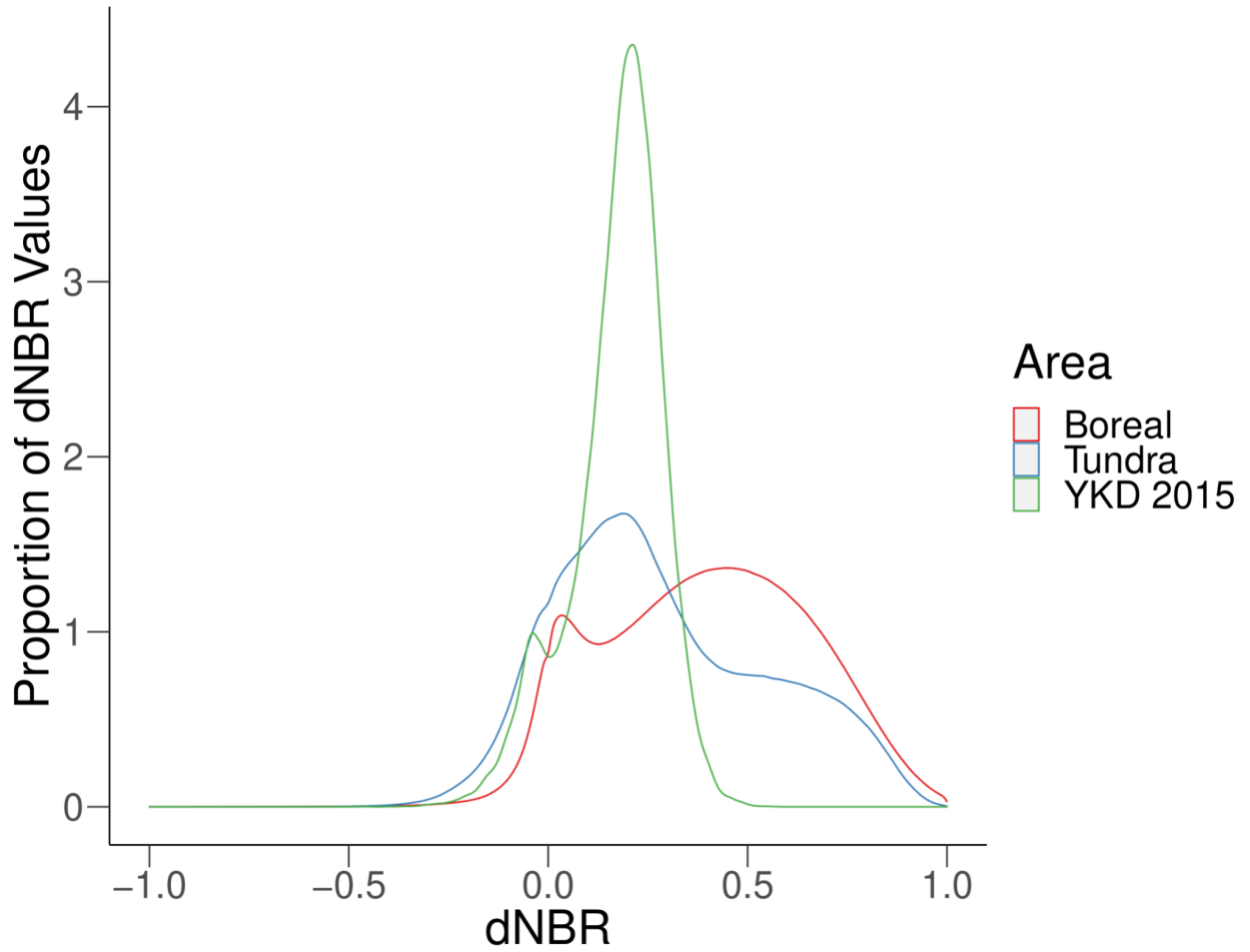
721

722 **Figure A8.** The distribution of dNBR values for the 2015 YKD fire season compared to all fires in boreal and tundra
723 systems in Alaska between the years 1989 and 2019.
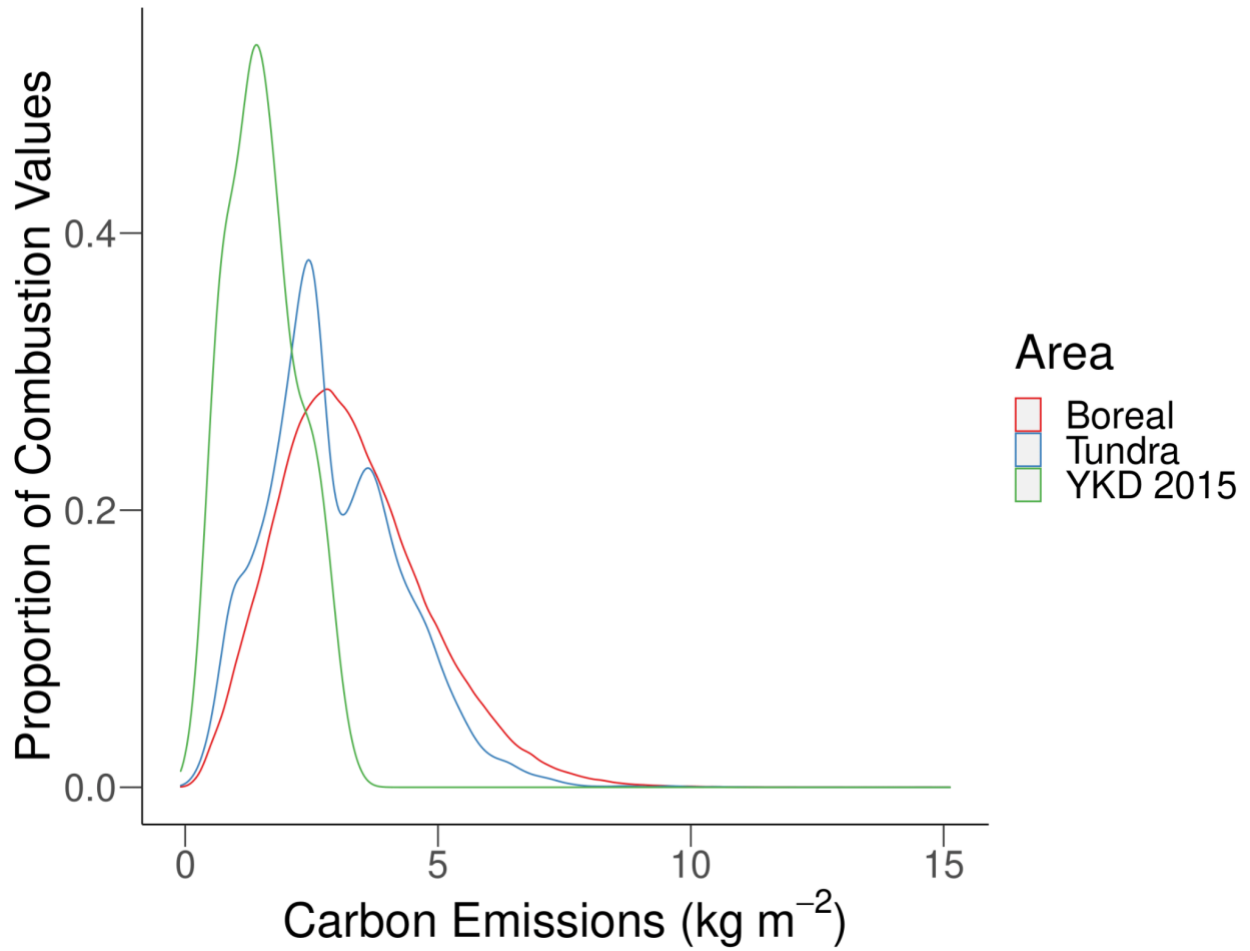
724
725 **Figure A9.** The distribution of carbon emission values from transect measurements in the YKD 2015 fires reported
726 herein and from remotely sensed pixels of all fires in boreal and tundra systems in Alaska between the years 2001
727 and 2018 (Scholten et al., 2021).

728
729
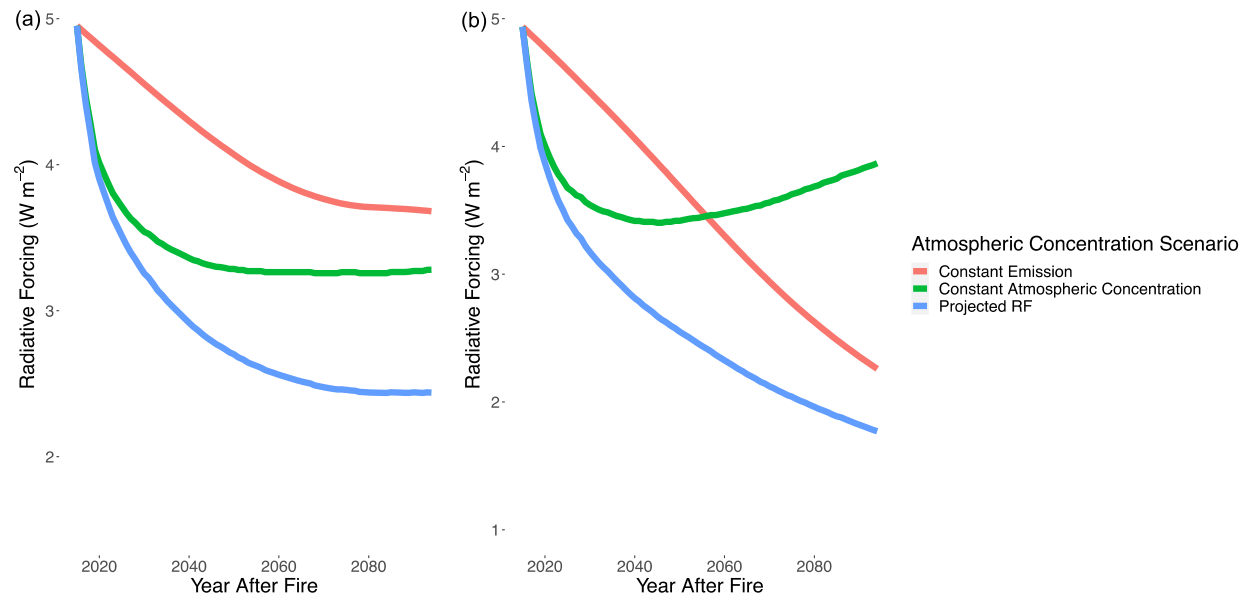
Figure A10. The radiative forcing of CO_2 emitted from the 2015 YKD fire season for RCP 4.5 (a) and 8.5 (b) when (i) holding the emission constant (red lines) so that no emitted CO_2 is sequestered, (ii) holding the background atmospheric concentration constant (green lines), and (iii) the combination of these, resulting in our main CO_2 radiative forcing equation (blue lines; Eq. 7). In the case of (i, red lines), increasing atmospheric CO_2 concentrations dampen the radiative impact of fire-emitted CO_2. In the case of (ii, green lines), the only time-varying impact on CO_2 radiative forcing is ocean and land sinks, which become less effective and even reverse with more extreme climate change according to model results presented in Joos et al. (2013). These lines are similar to the impulse response function of CO_2 for their respective scenarios in Joos et al. (2013).

Code and Data Availability

The radiative forcings calculation code is available on GitHub and Zenodo via DOI: 10.5281/zenodo.6617455

(Moubarak, 2022). All field and lab raw data used in this study, including vegetative reference point height

measurements and soil and vegetation core metrics, and combustion data products derived from our calculations are

publicly available in the NSF Arctic Data Center via DOI:10.18739/A2PR7MV5P (Moubarak et al., 2020).

Author Contributions

MM, BR, SS, and SN were involved with conceptualization, funding acquisition, and methodology. SP completed

investigation of burn severity data and jointly completed visualization with MM. MM, SS, and BR did investigation

of burn depth measurements and soil and vegetation characteristics. MM analyzed data and developed the radiative

forcings model. SS and SN did project administration for the field sampling. MM curated data and wrote the

original manuscript draft. MM, BR, SS, SP, and SN reviewed and edited the final published work.

Competing Interests

The authors declare that they have no conflict of interest.

Acknowledgements

754

755 This work was funded by the National Science Foundation (NSF-1915307 to SMN, NSF-1915307 to SS),

756 Casstevens Family Fund (to MM), and the National Aeronautics and Space Administration (NASA) Arctic-Boreal

757 Vulnerability Experiment (ABoVE; NNX15AU56A to BR) and the Gordon and Betty Moore Foundation (8414 to

758 SMN and BR). The authors would like to thank Dr. William Pfitsch for his helpful mentorship in the synthesis of

759 this project and creation of the written work. Also, the authors would like to thank Dr. Catherine Beck for offering

760 her knowledge about radiocarbon sample preparation and analysis.

References

762 Akagi, S. K., Yokelson, R. J., Wiedinmyer, C., Alvarado, M. J., Reid, J. S., Karl, T., Crounse, J. D. and Wennberg,
763 P. O.: Emission factors for open and domestic biomass burning for use in atmospheric models, Atmospheric
764 Chemistry and Physics, 11, 4039-4072, https://doi.org/10.5194/acp-11-4039-2011, 2011.

765 Barrett, K., Rocha, A. V., van de Weg, Martine Janet and Shaver, G.: Vegetation shifts observed in arctic tundra 17
766 years after fire, Remote Sensing Letters, 3, 729-736, https://doi.org/10.1080/2150704X.2012.676741, 2012.

767 Belshe, E. F., Schuur, E. and Bolker, B. M.: Tundra ecosystems observed to be CO_2 sources due to differential
768 amplification of the carbon cycle, Ecol. Lett., 16, 1307-1315, https://doi.org/10.1111/ele.12164, 2013.

769 Bieniek, P. A., Bhatt, U. S., York, A., Walsh, J. E., Lader, R., Strader, H., Ziel, R., Jandt, R. R. and Thoman, R. L.:
770 Lightning variability in dynamically downscaled simulations of Alaska's present and future summer climate, Journal
771 of Applied Meteorology and Climatology, 59, 1139-1152, https://doi.org/10.1175/JAMC-D-19-0209.1, 2020.

772 Boby, L. A., Schuur, E. A., Mack, M. C., Verbyla, D. and Johnstone, J. F.: Quantifying fire severity, carbon, and
773 nitrogen emissions in Alaska's boreal forest, Ecol. Appl., 20, 1633-1647, https://doi.org/10.1890/08-2295.1, 2010.

774 Bond, T. C., Zarzycki, C., Flanner, M. G. and Koch, D. M.: Quantifying immediate radiative forcing by black
775 carbon and organic matter with the Specific Forcing Pulse, Atmospheric Chemistry and Physics, 11, 1505-1525,
776 https://doi.org/10.5194/acp-11-1505-2011, 2011.

777 Chen, D., Loboda, T. V., and Hall, J. V.: A systematic evaluation of influence of image selection process on remote
778 sensing-based burn severity indices in North American boreal forest and tundra ecosystems, ISPRS Journal of
779 Photogrammetry and Remote Sensing, 159, 63-77, https://doi.org/10.1016/j.isprsjprs.2019.11.011, 2020a.

780 Chen, Y., Lara, M. J., and Hu, F. S.: A robust visible near-infrared index for fire severity mapping in Arctic tundra
781 ecosystems, ISPRS Journal of Photogrammetry and Remote Sensing, 159, 101-113,
782 https://doi.org/10.1016/j.isprsjprs.2019.11.012, 2020b.

783 Chen, Y., Li, Q., Randerson, J. T., Lyons, E. A., Kahn, R. A., Nelson, D. L. and Diner, D. J.: The sensitivity of CO
784 and aerosol transport to the temporal and vertical distribution of North American boreal fire emissions, Atmospheric
785 Chemistry and Physics, 9, 6559-6580, https://doi.org/10.5194/acp-9-6559-2009, 2009.

786 Chen, Y., Romps, D. M., Seeley, J. T., Veraverbeke, S., Riley, W. J., Mekonnen, Z. A. and Randerson, J. T.: Future
787 increases in Arctic lightning and fire risk for permafrost carbon, Nature Climate Change, 11, 404-410,
788 https://doi.org/10.1038/s41558-021-01011-y, 2021.

789 Cohen, J., Zhang, X., Francis, J., Jung, T., Kwok, R., Overland, J., Ballinger, T., Blackport, R., Bhatt, U. S. and
790 Chen, H.: Arctic change and possible influence on mid-latitude climate and weather: a US CLIVAR White Paper,
791 US CLIVAR reports, https://doi.org/10.5065/D6TH8KGW, 2018.

792 Collins, W. J., Fry, M. M., Yu, H., Fuglestvedt, J. S., Shindell, D. T. and West, J. J.: Global and regional
793 temperature-change potentials for near-term climate forcers, Atmospheric Chemistry and Physics, 13, 2471-2485,
794 https://doi.org/10.5194/acp-13-2471-2013, 2013.

795 Dieleman, C. M., Rogers, B. M., Potter, S., Veraverbeke, S., Johnstone, J. F., Laflamme, J., Solvik, K., Walker, X.
796 J., Mack, M. C. and Turetsky, M. R.: Wildfire combustion and carbon stocks in the southern Canadian boreal forest:
797 Implications for a warming world, Global Change Biol., 26, 6062-6079, https://doi.org/10.1111/gcb.15158, 2020.

798 Foga, S., Scaramuzza, P. L., Guo, S., Zhu, Z., Dilley, R. D., Beckmann, T., Schmidt, G. L., Dwyer, J. L., Joseph
799 Hughes, M., and Laue, B.: Cloud detection algorithm comparison and validation for operational Landsat data
800 products, Remote Sensing of Environment, 194, 379–390. https://doi.org/10.1016/j.rse.2017.03.026, 2017.

801 French, N. H., Whitley, M. A. and Jenkins, L. K.: Fire disturbance effects on land surface albedo in Alaskan tundra,
802 Journal of Geophysical Research: Biogeosciences, 121, 841-854, https://doi.org/10.1002/2015JG003177, 2016.
803
804 Frost, G. V., Loehman, R. A., Saperstein, L. B., Macander, M. J., Nelson, P. R., Paradis, D. P. and Natali, S. M.:
805 Multi-decadal patterns of vegetation succession after tundra fire on the Yukon-Kuskokwim Delta, Alaska,
806 Environmental Research Letters, 15, 025003, https://doi.org/10.1088/1748-9326/ab5f49, 2020.

807 Gorelick, N., Hancher, M., Dixon, M., Ilyushchenko, S., Thau, D. and Moore, R.: Google Earth Engine: Planetary-
808 scale geospatial analysis for everyone, Remote Sens. Environ., 202, 18-27, https://doi.org/10.1016/j.rse.2017.06.031,
809 2017.

810 He, J., Chen, D., Jenkins, L. and Loboda, T. V.: Impacts of wildfire and landscape factors on organic soil properties
811 in Arctic tussock tundra, Environmental Research Letters, 16, 085004, https://doi.org/10.1088/1748-9326/ac1192,
812 2021.

813 Holloway, J. E., Lewkowicz, A. G., Douglas, T. A., Li, X., Turetsky, M. R., Baltzer, J. L. and Jin, H.: Impact of
814 wildfire on permafrost landscapes: A review of recent advances and future prospects, Permafrost Periglacial
815 Processes, 31, 371-382, https://doi.org/10.1002/ppp.2048, 2020.

816 Hu, F. S., Higuera, P. E., Duffy, P., Chipman, M. L., Rocha, A. V., Young, A. M., Kelly, R. and Dietze, M. C.:
817 Arctic tundra fires: natural variability and responses to climate change, Frontiers in Ecology and the Environment,
818 13, 369-377, https://doi.org/10.1890/150063, 2015.

819 Hu, F. S., Higuera, P. E., Walsh, J. E., Chapman, W. L., Duffy, P. A., Brubaker, L. B. and Chipman, M. L.: Tundra
820 burning in Alaska: linkages to climatic change and sea ice retreat, Journal of Geophysical Research: Biogeosciences,
821 115, https://doi.org/10.1029/2009JG001270, 2010.

822 Hua, Q., Barbetti, M. and Rakowski, A. Z.: Atmospheric radiocarbon for the period 1950–2010, Radiocarbon, 55,
823 2059-2072, https://doi.org/10.2458/azu_js_rc.v55i2.16177, 2013.

824 Huang, S., Liu, H., Dahal, D., Jin, S., Li, S. and Liu, S.: Spatial variations in immediate greenhouse gases and
825 aerosol emissions and resulting radiative forcing from wildfires in interior Alaska, Theoretical and applied
826 climatology, 123, 581-592, https://doi.org/10.1007/s00704-015-1379-0, 2016.

827 IPCC: Climate Change 2021: The Physical Science Basis, Contribution of Working Group I to the Sixth Assessment
828 Report of the Intergovernmental Panel on Climate Change, edited by: Masson-Delmotte, V., Zhai, P., Pirani, A.,
829 Connors, S.L., Péan, C., Berger, S., Caud, N., Chen, Y., Goldfarb, L., Gomis, M.I., Huang, M., Leitzell, K., Lonnoy,
830 E., Matthews, J.B.R., Maycock, T.K., Waterfield, T., Yelekçi, O., Yu, R. and Zhou, B., Cambridge University Press,
831 Cambridge, United Kingdom and New York, NY, USA, In press, https://doi.org/10.1017/9781009157896, 2021.
832
833 Jafarov, E. E., Romanovsky, V. E., Genet, H., McGuire, A. D. and Marchenko, S. S.: The effects of fire on the
834 thermal stability of permafrost in lowland and upland black spruce forests of interior Alaska in a changing climate,
835 Environmental Research Letters, 8, 035030, https://doi.org/10.1088/1748-9326/8/3/035030, 2013.

836 Jaffe, D. A. and Wigder, N. L.: Ozone production from wildfires: A critical review, Atmos. Environ., 51, 1-10,
837 https://doi.org/10.1016/j.atmosenv.2011.11.063, 2012.

838 Joly, K., Duffy, P. A. and Rupp, T. S.: Simulating the effects of climate change on fire regimes in Arctic biomes:
839 implications for caribou and moose habitat, Ecosphere, 3, 1-18, https://doi.org/10.1890/ES12-00012.1, 2012.
840

841 Jones, B. M., Grosse, G., Arp, C. D., Miller, E., Liu, L., Hayes, D. J. and Larsen, C. F.: Recent Arctic tundra fire
842 initiates widespread thermokarst development, Scientific reports, 5, 1-13, https://doi.org/10.1038/srep15865, 2015.
843

844 Jones, B. M., Kolden, C. A., Jandt, R., Abatzoglou, J. T., Urban, F. and Arp, C. D.: Fire behavior, weather, and burn
845 severity of the 2007 Anaktuvuk River tundra fire, North Slope, Alaska, Arctic, Antarctic, and Alpine Research, 41,
846 309-316, https://doi.org/10.1657/1938-4246-41.3.309, 2009.
847

848 Joos, F., Roth, R., Fuglestvedt, J. S., Peters, G. P., Enting, I. G., Bloh, W. v., Brovkin, V., Burke, E. J., Eby, M. and
849 Edwards, N. R.: Carbon dioxide and climate impulse response functions for the computation of greenhouse gas
850 metrics: a multi-model analysis, Atmospheric Chemistry and Physics, 13, 2793-2825, https://doi.org/10.5194/acp-
851 13-2793-2013, 2013.

852 Jorgenson, M. T.: Hierarchical organization of ecosystems at multiple spatial scales on the Yukon-Kuskokwim
853 Delta, Alaska, USA, Arct. Antarct. Alp. Res., 32, 221-239, https://doi.org/10.1080/15230430.2000.12003360, 2000.

854 Kasischke, E. S., Williams, D. and Barry, D.: Analysis of the patterns of large fires in the boreal forest region of
855 Alaska. International Journal of Wildland Fire, 11, 131–144, https://doi.org/10.1071/wf02023, 2002.

856 Key, C. H. and Benson, N. C.: Landscape assessment (LA), In: Lutes, Duncan C.; Keane, Robert E.; Caratti, John
857 F.; Key, Carl H.; Benson, Nathan C.; Sutherland, Steve; Gangi, Larry J.2006.FIREMON: Fire effects monitoring
858 and inventory system. Gen. Tech. Rep. RMRS-GTR-164-CD. Fort Collins, CO: US Department of Agriculture,
859 Forest Service, Rocky Mountain Research Station.p.LA-1-55, 164, https://www.fs.usda.gov/treesearch/pubs/24066,
860 2006.

861 Kimball, J. S., Zhao, M., McDonald, K. C. and Running, S. W.: Satellite remote sensing of terrestrial net primary
862 production for the pan-Arctic basin and Alaska, Mitigation Adapt. Strat. Global Change, 11, 783-804,
863 https://doi.org/10.1007/s11027-005-9014-5, 2006.

864 Lindgren, A., Hugelius, G. and Kuhry, P.: Extensive loss of past permafrost carbon but a net accumulation into
865 present-day soils, Nature, 560, 219-222, https://doi.org/10.1038/s41586-018-0371-0, 2018.

866 Loboda, T. V., French, N. H., Hight-Harf, C., Jenkins, L., and Miller, M. E.: Mapping fire extent and burn severity
867 in Alaskan tussock tundra: An analysis of the spectral response of tundra vegetation to wildland fire, Remote
868 Sensing of Environment, 134, 194-209, https://doi.org/10.1016/j.rse.2013.03.003, 2013.

869 Lyons, E. A., Jin, Y. and Randerson, J. T.: Changes in surface albedo after fire in boreal forest ecosystems of
870 interior Alaska assessed using MODIS satellite observations, Journal of Geophysical Research: Biogeosciences,
871 113, https://doi.org/10.1029/2007JG000606, 2008.

872 Ma, S., He, F., Tian, D., Zou, D., Yan, Z., Yang, Y., Zhou, T., Huang, K., Shen, H. and Fang, J.: Variations and
873 determinants of carbon content in plants: a global synthesis, Biogeosciences, 15, 693-702,
874 https://doi.org/10.5194/bg-15-693-2018, 2018.

875 Mack, M. C., Bret-Harte, M. S., Hollingsworth, T. N., Jandt, R. R., Schuur, E. A., Shaver, G. R. and Verbyla, D. L.:
876 Carbon loss from an unprecedented Arctic tundra wildfire, Nature, 475, 489-492,
877 https://doi.org/10.1038/nature10283, 2011.

878 Meinshausen, M., Smith, S. J., Calvin, K., Daniel, J. S., Kainuma, M. L., Lamarque, J., Matsumoto, K., Montzka, S.
879 A., Raper, S. C. and Riahi, K.: The RCP greenhouse gas concentrations and their extensions from 1765 to 2300,
880 Clim. Change, 109, 213-241, https://doi.org/10.1007/s10584-011-0156-z, 2011.

881 Moubarak, M.: Radiative forcings of gaseous emissions, Zenodo [code], https://doi.org/10.5281/zenodo.6617455,
882 2022.

883   Moubarak, M., Sistla, S. and Natali, S. M.: Yukon-Kuskokwim River Delta 2015 fire burn depth measurements and
884   unburned soil and vegetation organic matter and carbon content collected in 2019, Arctic Data Center [data set],
885   https://doi.org/10.18739/A2DN3ZX3Q, 2020.

886   Myhre, G., Highwood, E. J., Shine, K. P. and Stordal, F.: New estimates of radiative forcing due to well mixed
887   greenhouse gases, Geophys. Res. Lett., 25, 2715-2718, https://doi.org/10.1029/98GL01908, 1998.

888   Myhre, G., Shindell, D., Bréon, F.-M., Collins, W., Fuglestvedt, J., Huang, J., Koch, D., Lamarque, J.-F., Lee, D.,
889   Mendoza, B., Nakajima, T., Robock, A., Stephens, G., Takemura, T., and Zhang, H.: Anthropogenic and Natural
890   Radiative Forcing, in: Climate Change: The Physical Science Basis. Contribution of Working Group I to the Fifth
891   Assessment Report of the Intergovernmental Panel on Climate Change, edited by: Stocker, T.F., Qin, D., Plattner,
892   G.-K., Tignor, M., Allen, S.K., Boschung, J., Nauels, A., Xia, Y., Bex, V. and Midgley, P.M., Cambridge University
893   Press, Cambridge, United Kingdom and New York, NY, USA, 659–740, https://doi.org/10.1017/
894   CBO9781107415324.018, 2013.
895
896   Natali, S. M., Schuur, E. A., Mauritz, M., Schade, J. D., Celis, G., Crummer, K. G., Johnston, C., Krapek, J.,
897   Pegoraro, E. and Salmon, V. G.: Permafrost thaw and soil moisture driving CO2 and CH4 release from upland
898   tundra, Journal of Geophysical Research: Biogeosciences, 120, 525-537, https://doi.org/10.1002/2014JG002872,
899   2015.

900   Natali, S. M., Watts, J. D., Rogers, B. M., Potter, S., Ludwig, S. M., Selbmann, A., Sullivan, P. F., Abbott, B. W.,
901   Arndt, K. A. and Birch, L.: Large loss of CO 2 in winter observed across the northern permafrost region, Nature
902   Climate Change, 9, 852-857, https://doi.org/10.1038/s41558-019-0592-8, 2019.

903   O'Halloran, T. L., Law, B. E., Goulden, M. L., Wang, Z., Barr, J. G., Schaaf, C., Brown, M., Fuentes, J. D.,
904   Göckede, M. and Black, A.: Radiative forcing of natural forest disturbances, Global Change Biol., 18, 555-565,
905   https://doi.org/10.1111/j.1365-2486.2011.02577.x, 2012.

906   Pinheiro J, Bates D, DebRoy S, Sarkar D, and R Core Team: nlme: Linear and Nonlinear Mixed Effects Models, R
907   package version 3.1-149, https://CRAN.R-project.org/package=nlme, 2020.
908
909   Potter, S., Solvik, K., Erb, A., Goetz, S. J., Johnstone, J. F., Mack, M. C., Randerson, J. T., Román, M. O., Schaaf,
910   C. L. and Turetsky, M. R.: Climate change decreases the cooling effect from postfire albedo in boreal North
911   America, Global Change Biol., 26, 1592-1607, https://doi.org/10.1111/gcb.14888, 2020.

912   Potter, S., Veraverbeke, S., Walker, X. J., Mack, M. C., Goetz, S. J., Baltzer, J. L., Dieleman, C., French, N. H. F.,
913   Kane, E. S., Turetsky, M. R., Wiggins, E. B., and Rogers, B. M.: ABoVE: Burned Area, Depth, and Combustion for
914   Alaska and Canada, 2001-2019, ORNL DAAC, Oak Ridge, Tennessee, USA [data set],
915   https://doi.org/10.3334/ORNLDAAC/2063, 2022.

916   Quinn, P. K., Bates, T. S., Baum, E., Doubleday, N., Fiore, A. M., Flanner, M., Fridlind, A., Garrett, T. J., Koch, D.
917   and Menon, S.: Short-lived pollutants in the Arctic: their climate impact and possible mitigation strategies,
918   Atmospheric Chemistry and Physics, 8, 1723-1735, https://doi.org/10.5194/acp-8-1723-2008, 2008.

919   R Core Team: R: A language and environment for statistical computing, R Foundation for Statistical Computing,
920   Vienna, Austria, https://www.R-project.org/, 2020.
921
922   Ramsey, C. B.: Bayesian analysis of radiocarbon dates, Radiocarbon, 51, 337-360,
923   https://doi.org/10.1017/S0033822200033865, 2009.

924   Randerson, J. T., Liu, H., Flanner, M. G., Chambers, S. D., Jin, Y., Hess, P. G., Pfister, G., Mack, M. C., Treseder,
925   K. K. and Welp, L. R.: The impact of boreal forest fire on climate warming, Science, 314, 1130-1132,
926   https://doi.org/10.1126/science.1132075, 2006.

927   Raynolds, M. K., Walker, D. A. and Maier, H. A.: Plant community-level mapping of arctic Alaska based on the
928   Circumpolar Arctic Vegetation Map, Phytocoenologia, 35, 821, https://doi.org/10.1127/0340-269X/2005/0035-
929   0821, 2005.

930 Reimer, P. J., Brown, T. A. and Reimer, R. W.: Discussion: reporting and calibration of post-bomb 14C data,
931 Radiocarbon, 46, 1299-1304, https://doi.org/10.1017/S0033822200033154, 2004.

932 Rocha, A. V., Loranty, M. M., Higuera, P. E., Mack, M. C., Hu, F. S., Jones, B. M., Breen, A. L., Rastetter, E. B.,
933 Goetz, S. J. and Shaver, G. R.: The footprint of Alaskan tundra fires during the past half-century: implications for
934 surface properties and radiative forcing, Environmental Research Letters, 7, 044039, https://doi.org/10.1088/1748-
935 9326/7/4/044039, 2012.

936 Rocha, A. V. and Shaver, G. R.: Burn severity influences postfire CO2 exchange in arctic tundra, Ecol. Appl., 21,
937 477-489, https://doi.org/10.1890/10-0255.1, 2011a.

938 Rocha, A. V. and Shaver, G. R.: Postfire energy exchange in arctic tundra: the importance and climatic implications
939 of burn severity, Global Change Biol., 17, 2831-2841, https://doi.org/10.1111/j.1365-2486.2011.02441.x, 2011b.

940 Rogers, B. M., Randerson, J. T. and Bonan, G. B.: High-latitude cooling associated with landscape changes from
941 North American boreal forest fires, Biogeosciences, 10, 699-718, https://doi.org/10.5194/bg-10-699-2013, 2013.

942 Rogers, B. M., Veraverbeke, S., Azzari, G., Czimczik, C. I., Holden, S. R., Mouteva, G. O., Sedano, F., Treseder, K.
943 K. and Randerson, J. T.: Quantifying fire-wide carbon emissions in interior Alaska using field measurements and
944 Landsat imagery, Journal of Geophysical Research: Biogeosciences, 119, 1608-1629,
945 https://doi.org/10.1002/2014JG002657, 2014.

946 Roy, D. P., Kovalskyy, V., Zhang, H. K., Vermote, E. F., Yan, L., Kumar, S. S. and Egorov, A.: Characterization of
947 Landsat-7 to Landsat-8 reflective wavelength and normalized difference vegetation index continuity. Remote
948 Sensing of Environment, 185, 57–70, https://doi.org/10.1016/j.rse.2015.12.024, 2016.

949 Sae-Lim, J., Russell, J. M., Vachula, R. S., Holmes, R. M., Mann, P. J., Schade, J. D. and Natali, S. M.:
950 Temperature-controlled tundra fire severity and frequency during the last millennium in the Yukon-Kuskokwim
951 Delta, Alaska, The Holocene, 29, 1223-1233, https://doi.org/10.1177/0959683619838036, 2019.

952 Scholten, R.C., S. Veraverbeke, R. Jandt, E.A. Miller, and B.M. Rogers.: ABoVE: Ignitions, Burned Area, and
953 Emissions of Fires in AK, YT, and NWT, 2001-2018, ORNL DAAC, Oak Ridge, Tennessee, USA [data set],
954 https://doi.org/10.3334/ORNLDAAC/1812, 2021.

955 Schuur, E. A., McGuire, A. D., Schädel, C., Grosse, G., Harden, J. W., Hayes, D. J., Hugelius, G., Koven, C. D.,
956 Kuhry, P. and Lawrence, D. M.: Climate change and the permafrost carbon feedback, Nature, 520, 171-179,
957 https://doi.org/10.1038/nature14338, 2015.

958 Shaw, R. D.: An archaeology of the central Yupik: A regional overview for the Yukon-Kuskokwim Delta, northern
959 Bristol Bay, and Nunivak Island, Arctic Anthropology, 234-246, http://www.jstor.org/stable/40316467, 1998.

960 U.S Environmental Protection Agency: NA Eco Level 1, U.S. EPA Office of Research & Development (ORD) -
961 National Health and Environmental Effects Research Laboratory (NHEERL) [data set], https://www.epa.gov/eco-
962 research/ecoregions-north-america, 2010.

963 Virkkala, A., Aalto, J., Rogers, B. M., Tagesson, T., Treat, C. C., Natali, S. M., Watts, J. D., Potter, S., Lehtonen, A.
964 and Mauritz, M.: Statistical upscaling of ecosystem CO2 fluxes across the terrestrial tundra and boreal domain:
965 Regional patterns and uncertainties, Global Change Biol., 27, 4040-4059, https://doi.org/10.1111/gcb.15659, 2021.

966 Veraverbeke, S., Rogers, B. M., and Randerson, J. T.: CARVE: Alaskan Fire Emissions Database (AKFED), 2001-
967 2013, ORNL DAAC, Oak Ridge, Tennessee, USA [data set], https://doi.org/10.3334/ORNLDAAC/1282, 2015a.

968 Veraverbeke, S., Rogers, B. M. and Randerson, J. T.: Daily burned area and carbon emissions from boreal fires in
969 Alaska, Biogeosciences, 12, 3579-3601, https://doi.org/10.5194/bg-12-3579-2015, 2015b.

970 Veraverbeke, S., Delcourt, C. J., Kukavskaya, E., Mack, M., Walker, X., Hessilt, T., Rogers, B. and Scholten, R. C.:
971 Direct and longer-term carbon emissions from arctic-boreal fires: a short review of recent advances, Current
972 Opinion in Environmental Science & Health, 23, 100277, https://doi.org/10.1016/j.coesh.2021.100277, 2021.

Veraverbeke, S., Rogers, B. M., Goulden, M. L., Jandt, R., Miller, C. E., Wiggins, E. B., and Randerson, J. T.: ABoVE: Ignitions, burned area and emissions of fires in AK, YT, and NWT, 2001-2015, ORNL DAAC, Oak Ridge, Tennessee, USA [data set], https://doi.org/10.3334/ORNLDAAC/1341, 2017a.

Veraverbeke, S., Rogers, B. M., Goulden, M. L., Jandt, R. R., Miller, C. E., Wiggins, E. B. and Randerson, J. T.: Lightning as a major driver of recent large fire years in North American boreal forests, Nature Climate Change, 7, 529-534, https://doi.org/10.1038/nclimate3329, 2017b.

Walker, X. J., Baltzer, J. L., Bourgeau-Chavez, L. L., Day, N. J., De groot, W. J., Dieleman, C., Hoy, E. F., Johnstone, J. F., Kane, E. S. and Parisien, M. A.: ABoVE: Synthesis of Burned and Unburned Forest Site Data, AK and Canada, 1983-2016, ORNL DAAC, https://doi.org/10.3334/ORNLDAAC/1744, 2020a.

Walker, X. J., Rogers, B. M., Veraverbeke, S., Johnstone, J. F., Baltzer, J. L., Barrett, K., Bourgeau-Chavez, L., Day, N. J., de Groot, W. J. and Dieleman, C. M.: Fuel availability not fire weather controls boreal wildfire severity and carbon emissions, Nature Climate Change, 10, 1130-1136, https://doi.org/10.1038/s41558-020-00920-8, 2020b.

Walker, X. J., Baltzer, J. L., Bourgeau-Chavez, L., Day, N. J., Dieleman, C. M., Johnstone, J. F., Kane, E. S., Rogers, B. M., Turetsky, M. R. and Veraverbeke, S.: Patterns of ecosystem structure and wildfire carbon combustion across six ecoregions of the North American boreal forest, Frontiers in Forests and Global Change, 3, 87, https://doi.org/10.3389/ffgc.2020.00087, 2020c.

Walker, X. J., Baltzer, J. L., Cumming, S. G., Day, N. J., Ebert, C., Goetz, S., Johnstone, J. F., Potter, S., Rogers, B. M. and Schuur, E. A.: Increasing wildfires threaten historic carbon sink of boreal forest soils, Nature, 572, 520-523, https://doi.org/10.1038/s41586-019-1474-y, 2019.

Walker, X. J., Baltzer, J. L., Cumming, S. G., Day, N. J., Johnstone, J. F., Rogers, B. M., Solvik, K., Turetsky, M. R. and Mack, M. C.: Soil organic layer combustion in boreal black spruce and jack pine stands of the Northwest Territories, Canada, Int. J. Wildland Fire, 27, 125-134, https://doi.org/10.1071/WF17095, 2018a.

Walker, X. J., Rogers, B. M., Baltzer, J. L., Cumming, S. G., Day, N. J., Goetz, S. J., Johnstone, J. F., Schuur, E. A., Turetsky, M. R. and Mack, M. C.: Cross-scale controls on carbon emissions from boreal forest megafires, Global Change Biol., 24, 4251-4265, https://doi.org/10.1111/gcb.14287, 2018b.

Ward, D. S., Kloster, S., Mahowald, N. M., Rogers, B. M., Randerson, J. T. and Hess, P. G.: The changing radiative forcing of fires: global model estimates for past, present and future, Atmospheric Chemistry and Physics, 12, 10857-10886, https://doi.org/10.5194/acp-12-10857-2012, 2012.

Wiggins, E. B., Veraverbeke, S., Henderson, J. M., Karion, A., Miller, J. B., Lindaas, J., Commane, R., Sweeney, C., Luus, K. A. and Tosca, M. G.: The influence of daily meteorology on boreal fire emissions and regional trace gas variability, Journal of Geophysical Research: Biogeosciences, 121, 2793-2810, https://doi.org/10.1002/2016JG003434, 2016.

Zhou, Z., Liu, L., Jiang, L., Feng, W. and Samsonov, S. V.: Using long-term SAR backscatter data to monitor post-fire vegetation recovery in tundra environment, Remote Sensing, 11, 2230, https://doi.org/10.3390/rs11192230, 2019.